Please cite the Published Version

A VOS based Immersed Boundary-Lattice Boltzmann method for incompressible fluid flows with complex and moving boundaries

Longfei Cong[*1,3], Bin Teng [1], Wei Bai [2], and Biaosong Chen [3]

[1]State Key Laboratory of Coastal and Offshore Engineering, Dalian University of Technology, Dalian 116024, China

[2]Department of Computing and Mathematics, Manchester Metropolitan University, Manchester M1 5GD, UK

[3]State Key Laboratory of Structural Analysis for Industrial Equipment, Dalian University of Technology, Dalian 116024, China

Abstract

A Volume of Solid (VOS) based Immersed Boundary-Lattice Boltzmann Method (IB-LBM) in the framework of the direct forcing based IB-LBM model has been developed in this work to simulate the fluid flow with complex and moving boundaries efficiently. In the present model, the concept of VOS is introduced to achieve the field extension to the solid phase, and a unified Lattice Boltzmann Equation (LBE) has been obtained to describe the fluid flow and the solid body motion consistently. To solve the resulting unified LBE, an efficient direct forcing model has been developed. Compared with the traditional surface based IB model with the direct forcing strategy, in the present work, the dependency of the Lagrangian grid to describe the body profile on the background Cartesian grid is removed by modelling the solid body with a Level-Set function. With such Level-Set description about the body surface, the VOS function can be obtained for the further field extension. With the present IB-LBM algorithm, the motion of the solid body can be enforced effectively without iterations about the forcing term compared with the implicit velocity correction or multiple velocity correction based IB algorithm, and flow penetration, which has been observed in the explicit velocity correction based IB model, can be reduced considerably. To achieve the velocity adjustment in the solid phase, an optimal forcing factor is recommended. With such optimal factor, the unphysical oscillation during force prediction can be well controlled. To verify the performance of the present model, a series of typical benchmarks, including the fluid flow caused by general shaped fixed or moving structures, hydrodynamic characteristics of thin-wall bodies undergoing specified motions and even more complex vortex induced vibrations, are conducted and the good agreements between the present results and the well-validated previous ones confirm the reliability and robustness of the present model.

Keywords: Immersed Boundary method; Lattice Boltzmann method; Direct forcing method; Level-Set function; Volume of Solid; Field extension

1 Introduction

As one of its main goals, the development of Computational Fluid Dynamics (CFD) aims to predict effectively the behaviors of fluid flows with complex boundaries. In addition to the complexity of the static boundary geometry, the term "complex" is also associated with the deformation or the rigid motion of boundary surfaces.

---

*Corresponding author: conglongfei@dlut.edu.cn

Compared with the well-developed Arbitrary Lagrange-Euler (ALE) algorithm, the Immersed Boundary (IB) method, or Embedded Boundary (EB) method, has attracted plenty of attention due to its advantages in the flexibility and relative ease to treat moving boundaries, especially with large deformations. Because of the local velocity correction process around the solid body embedded in the background Cartesian grid to account for its effect on the fluid flow, the IB model simplifies the flow prediction considerably, while avoids the possible breakdown of the simulation caused by the grid distortion.

As an extension of the original IB model (Peskin, 1972), the penalty IB (pIB) model (Goldstein et al., 1993; Huang et al., 2011; Tian et al., 2011) has been well developed to simulate the fluid flow around rigid or deformable bodies. With the introduction of user-defined penalty parameters to couple the feedback force, the body motion and the fluid flow, the resulting stiff problem limits the allowable time increment for a stable simulation. For the consideration about numerical stability and to remove the empirical parameters in the pIB model, Fadlun et al. (2000), Tseng and Ferziger (2003), Yang and Balaras (2006) and Mittal et al. (2008) developed the sharp interface direct forcing model, where the fluid velocity around the solid boundary is reconstructed by the bounded interpolation with the surrounding fluid and boundary nodes as the stencil to implicitly enforce the desirable no-slip boundary condition on the boundary surface. To remedy the numerical issues about the non-physical mass flux of fluid flow caused by the local velocity correction (Fadlun et al., 2000), Kim et al. (2001) and Huang and Sung (2007) introduced the mass source or mass sink inside the solid domain to balance the non-physical velocity divergence of fluid flow for flow prediction with improved accuracy around the solid boundary. Furthermore, various numerical technics have been developed to achieve such conservation correction (Kang et al., 2009; Seo and Mittal, 2011). Generally speaking, although the sharp interface IB method maintains the sharp interface between the solid and fluid phases without interface diffussion, the complicated geometrical calculation and the stencil-fitting for local velocity reconstruction make the overall algorithm complex, which limits the robustness of the model considerably.

Considering the attractive features of pIB model (flexibility in stencil-fitting for interpolation) and direct forcing model (excellent numerical stability), Uhlmann (2005) developed a diffused interface direct forcing based IB model. Within such IB framework, the forcing term for velocity correction is evaluated by the direct forcing model at the Lagrangian boundary points, rather than the Euler boundary points. With such strategy, numerical stability has be preserved compared with pIB model. Different from the sharp interface direct forcing model, the geometric-free kernel function based interpolation scheme further improves the robustness of the model.

In the traditional surface based diffused interface IB method (Uhlmann, 2005), the boundary surface of the solid body is presented by the discretized elements, and the forcing term is evaluated at the boundary nodes firstly and then spread to the surrounding Euler nodes for velocity correction. Without distribution matching between boundary nodes and background Euler nodes, flow leakage may occur (Zhao et al., 2021). In the explicit direct forcing model (Uhlmann, 2005), the spacing of the IB nodes can be set as small as possible to avoid flow leakage at the expense of computational cost. Meanwhile, within the implicit direct forcing framework, the dense distribution of IB nodes leads to numerical issues about singularity and instability (the matrix for velocity correction or forcing term can be ill-conditioned as shown in Pinelli et al. (2010)). Therefore, there is still no universal rule for the density of IB nodes in the diffused interface direct forcing model, and the grid setting is empirical.

As an alternative strategy, Pan (2006) and Arnab (2018) developed a volume based IB method to achieve the coupling between rigid motion and real fluid flow with a combination of these two motions with the Volume

of Solid (VOS) function as the weighting factor. It has been proven that such treatment is the first-order approximation of the Boundary Data Immersion method (BDIM) (Weymouth and Yue, 2011; Maertens and Weymouth, 2015). Within such diffused interface IB framework, the real fluid flow transits smoothly to the target solid state and the desirable boundary condition can be enforced implicitly (Nakayama and Yamamoto, 2005; Jafari et al., 2011).

In the numerical simulation of incompressible, or weak-compressible flows, the no-slip condition on the boundary surface and the divergence-free condition for the fluid flow are two separated constraints to the velocity field (Taira and Colonius, 2007; Li et al., 2016). To achieve their correct coupling, Taira and Colonius (2007) proposed the IB-projection model, where the pressure of the fluid flow, together with the Lagrangian forcing term on the IB boundary, are treated consistently as the Lagrangian multipliers to enforce the divergence-free and no-slip boundary conditions for the fluid flow. Other than the decoupling error (divergence-free and no-slip conditions for fluid flow) caused by the operator splitting to simplify the overall algorithm, the diffused interface direct forcing model also introduces an extra error during the kernel function based interpolation-spreading process (Gsell and Favier, 2021). As an extension of the work by Uhlmann (2005), Wang et al. (2008), Wu and Shu (2009) and Pinelli et al. (2010) conducted the multi-direct forcing and implicit direct forcing models respectively to remedy such interpolation-spreading related slip error.

Other than traditional incompressible Navier-Stokes solvers based on the finite volume method, finite difference method and finite element method, the Lattice Boltzmann Method (LBM), a weak-compressible Navier-Stokes solver, has become popular in the field of flow simulations and fluid-structure interactions, due to its second-order numerical accuracy, simple numerical scheme and resulting computational efficiency (Li and Lu, 2012; Hua et al., 2014; Peng et al., 2018a; Peng et al., 2018b; Cong et al., 2020). In the framework of LBM, the distribution function has been adopted to describe the fluid flow by statistic mechanics (Qian et al., 1992). Keeping the basic algorithm of LBM, in order to improve local accuracy about flow prediction, multi-grid models have been developed to achieve the space-time adaptive simulation of fluid flows (Chen et al., 2006; Rohde et al., 2006; Xu et al., 2018). As a natural extension, the diffused interface IB method has also been coupled with LBM to achieve an efficient flow simulation with solid body (Feng and Michaelides, 2005; Kang and Hassan, 2011; Favier et al., 2014; Wang et al., 2015; Wang et al., 2016).

To improve the efficiency of surface based direct forcing model, in the present work, a VOS based diffused interface direct forcing immersed boundary model is developed for numerical simulation about fluid flow with complex and moving boundaries. Within the present IB framework, the effects of solid phase on the fluid flow is modelled by an explicitly defined forcing term distributed inside the solid domain, rather than around the solid boundary only. Although forcing term iteration, which has been adopted in implicit direct forcing and multi-direct forcing model for accuarcy improvement, has been avoided in the present model, the no-slip condition can been well enforced on the boundary of the solid domain. Compared with the surface based IB model, in the present model, the surface discretization process is removed for the solid body with simple geometries. While for the solid body with complex boundaries, the surface mesh is only needed to construct the Level-Set function and doesn't need to match the background Euler grid. As one of its attractive features, the present model eliminates the dependency of the Lagrangian grid distribution on the resolution of the background Euler grid, thus preventing the flow leakage and diminishing the slip error. In addition, as the velocity is evaluated at the Euler points, the interpolation process has been omitted, avoiding the relating interpolation error. With the IB force distributed in the whole solid domain and an optimal forcing factor for the evaluation of forcing term,

a physical pressure extension to the solid phase has be obtained, which is helpful to control the non-physical force oscillation in Fluid-Structure Interactions (FSI). Furthermore, to evaluate the hydrodynamic loading on the structure, an indirect formulation without surface integral is developed and the rigid body assumption for the force correction is proved for all the rigid motion modes. By the introduction of the concept of multi-grid to achieve the adaptive flow simulation, the local accuracy in the near field of the structure has been maintained efficiently. Several numerical tests are conducted and extensive comparisons are carried out to validate the accuracy and robustness of the present IB strategy and its coupling with LBM.

2 Numerical methods for fluid flow and rigid body motion

2.1 Governing equations

In the present work, a global coordinate system $o - xy$ is adopted and the flow variations are defined with respect to this Cartesian coordinate system. The viscous fluid flow can be described by the Navier-Stokes (NS) equations, which include both the momentum balancing and the mass conservation equations:

$$U_t + (U \cdot \nabla)U = -\frac{1}{\rho_f}\nabla P + \nu\nabla^2 U,$$
$$\nabla \cdot U = 0, \tag{1}$$

where U denotes the velocity vector, P the pressure, t the time, ρ_f the fluid density and ν the kinematic viscous coefficient. In addition, only the solid body with rigid motions is considered in the present work, and the motion of the solid body defined on its mass centre can be described with the Newton's second law,

$$m\ddot{X}_c = F_x, \qquad m\ddot{Y}_c = F_y, \qquad I\ddot{\theta}_c = M, \tag{2}$$

where m and I are the mass of the body and its inertial moment about mass centre respectively. X_c, Y_c and θ_c denote the translational displacements in the x and y directions and the rotational displacement of the body about its mass centre, and F_x, F_y and M are the corresponding forces and moment.

2.2 Lattice Boltzmann method for fluid flow

In traditional macro-scale NS solvers, the fractional-step method is always adopted to decouple the pressure and velocity of fluid flow to enforce the mass conservation and momentum balancing, which imposes the challenge in solving the resultant Poisson-type equation. To resolve the fluid flow efficiently, the Lattice Boltzmann Method (LBM) is adopted in the present work, in which the incompressible fluid is treated as a weak-compressible one. In the framework of LBM, the flow field is described by the distribution function, which relates to the amount of particles with a particular velocity in a unit volume (e.g., $q_\alpha(x, t^n) = \hat{q}(x, t^n; v = e_\alpha)$) denotes the amount of particles in the unit volume around $X = x$ at $t = t^n$ with the velocity $v = e_\alpha$ in the meso-scopic scale) and obeys the Lattice Boltzmann Equation (LBE). In the macro-scale, the density and momentum of the fluid flow can be obtained by the statistics of such distribution function directly (Qian et al., 1992).

In the framework of LBM, the evolution of the distribution function follows two separated steps: (a) at certain time $t = t^n$, the distribution function firstly experiences its collision stage $q_\alpha^*(x, t^n) = q_\alpha(x, t^n) + \Omega_\alpha$,

where Ω_α denotes the collision operator; (b) after the collision operation, the particle at $t = t^n$ and $X = x$ moves to its neighbouring grid node, i.e., $q_\alpha(x + e_\alpha \delta t, t^{n+1}) = q_\alpha^*(x, t^n)$, and such stage is named as streaming. To simplify the complexity and nonlinearity of the collision operator, based on the assumption that q_α is a perturbation about its equilibrium state q_α^{eq} and the observation that the effect of Ω_α is to drive q_α to its equilibrium state, the collision operator can be linearised with Single Relaxation Time (SRT) model: $\Omega_\alpha = (q_\alpha^{eq} - q_\alpha)/\tau$, where τ denotes the nondimensional relaxation rate(Chen et al., 1991; Qian et al., 1992). To improve the performance of LBM, especially for cases with moderate to high Reynolds numbers, the Multiple Relaxation Time (MRT) model (Lallemand and Luo, 2000) has become popular for its excellent numerical stability.

Considering its improved numerical stability, in the present work, the MRT model is adopted as the collision operator and the Lattice Boltzmann equations with such collision model can be written as

$$
q_\alpha(x + e_\alpha \delta t, t_n + \delta t) - q_\alpha(x, t_n) = -M^{-1} \cdot S \cdot M \cdot (\mathbf{Q} - \mathbf{Q}^{eq}) \Big|_\alpha ,
$$
$$
\mathbf{Q}^{eq} \Big|_\alpha = \rho_f \omega_\alpha \left[1 + \frac{e_\alpha \cdot u}{c_s^2} + \frac{(e_\alpha \cdot u)^2}{2c_s^4} - \frac{u \cdot u}{2c_s^2} \right], \tag{3}
$$

where q_α denotes the distribution function with $v = e_\alpha$, $\mathbf{Q} = (q_1, q_2, ...)$ is a vector consisting of q_αs, the symbol $(\cdot)^{eq}$ denotes the equilibrium state, M is the transformation matrix to achieve the mapping from the meso-scopic scale distribution functions to their macro-scale moments, and M^{-1} is the matrix for the backward transformation. In the present 2D case, the D2Q9 model is adopted as the lattice model (Qian et al., 1992). To execute the collision operator, S is a diagonal matrix, which contains different relaxation rates to drive the moments to their equilibrium states, and the diagonal elements of the matrix are set by following the work in Fakhari and Lee (2013) for an improved numerical stability, especially for cases with larger Re. In the definition of the equilibrium distribution functions, c_s denotes the sound velocity of the fluid and its value relates to the grid spacing and the time increment by $c_s = \frac{\delta x}{\sqrt{3}\delta t}$. Furthermore, ρ_f and u are the density and velocity of the fluid flow respectively and can be evaluated by

$$
\rho_f = \sum_\alpha q_\alpha, \qquad \rho_f u = \sum_\alpha e_\alpha q_\alpha. \tag{4}
$$

According to the multi-scale analysis about the LBE, if the pressure of the fluid flow depends on the density of the fluid explicitly by $P = (\rho_f - \rho_0)c_s^2$, where ρ_0 is the reference value of the fluid density, i.e., the density of the fluid flow without disturbance, the macro-scale behaviour of the fluid flow recovers to the NS equation with an error $O(Ma^3)$, where Ma is defined by the reference velocity and the local sound speed as $Ma = |U_{ref}|/c_s$.

In addition, to resolve the fluid flow in detail with local high resolution, a multi-grid technique is adopted in the present work, where the computational domain is covered by rectangular patches with different grid spacings, as shown in Fig. 1(a). To keep a consistent c_s among patches with different grid spacings, the time increment δt matches the grid spacing by $\delta t_{fine}/\delta t_{coarse} = \delta x_{fine}/\delta x_{coarse}$. To simplify the data synthetics between patches with different spacings, the refinement ratio between two levels of patches is set as $\delta x_{fine}/\delta x_{coarse} = \frac{1}{2}$. Therefore, the flow field is firstly resolved on the coarse grid, and then followed by two steps of flow predictions on the fine grid.

Before the fluid flow is predicted on the fine grid, the interpolation for the buffer data with that on the coarse grid is carried out firstly ((a) and (b) in Fig. 1(b)). Using those values as the boundary condition, the

LB algorithm can be conducted on the fine grid in its usual manner ((c) in Fig. 1(b)). Once the solution on the fine grid is available, the coarse grid solution is recovered where it is overlapped with the fine grid ((d) in Fig. 1(b)). As it can be observed, the aforementioned sequences shown in Fig. 1(b) couple the flow fields on the fine grid and the coarse grid strongly. In the present work, the space-time multi-scale LBM (Rohde et al., 2006) is used for its better conservation characteristics.
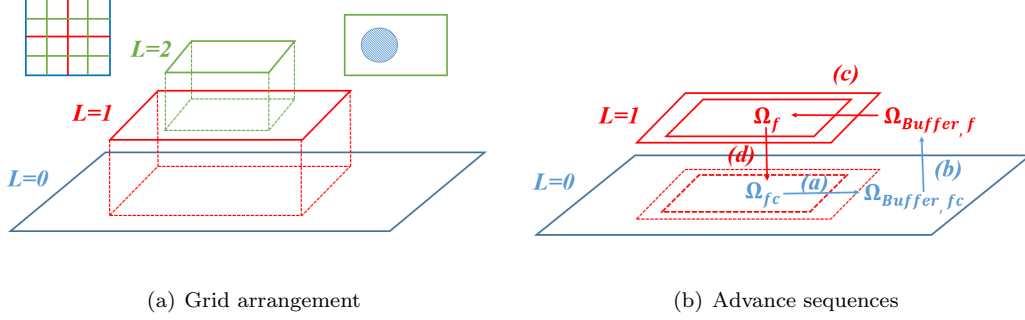

(a) Grid arrangement

(b) Advance sequences

Fig. 1. Sketch of the multi-grid space-time adaptive Lattice Boltzmann model.

3 Volume of Solid (VOS) based Immersed Boundary method for fluid-structure coupling

To account for the effect of the solid body on the fluid flow, the diffused interface IB model is adopted in the present work based on the direct forcing strategy. In difference to the surface based direct forcing model, where the surface mesh is adopted to describe the profile of the solid body, in the present model, the solid body is treated in a similar way as the well-known Volume of Fluid (VOF) model to capture the interface between two phases. In this method, for a given grid point, a Volume of Solid (VOS) function α is defined to represent the ratio of the solid which is contained in a certain control volume, that is

$$
\begin{cases}
\alpha = 1 & \text{for solid cell} \\
\alpha = 0 & \text{for fluid cell} \\
0 < \alpha < 1 & \text{for interface cell}
\end{cases}
\tag{5}
$$

In its original form, the VOS function changes sharply in the interface region and this characteristic challenges the robustness of the numerical solver. To improve the stability of the solver, the sharp interface between the fluid and solid phases is smoothed out in a transition region across a few grid layers. The typical width of the interface is $2\Delta/\delta x = 4$, where Δ is the half-width of the diffused interface, and δx denotes the typical grid spacing. To achieve such smoothing, a Level-Set (LS) function ϕ is defined on a given grid point, which is in the form of the signed distance function, and it is defined as the minimum distance from the grid point to the surface of the solid body. If the grid point is inside the solid body, the LS function is defined to be negative, while if the grid point is in the fluid region, its value is positive. With the well-defined LS function, the VOS function α can be defined with the smooth version of the Heaviside function,

$$\alpha = \begin{cases} 1, & \phi < -\Delta \\ 1 - \frac{1 + \phi/\Delta + sin(\pi\phi/\Delta)/\pi}{2}, & -\Delta \leq \phi \leq +\Delta \\ 0, & \phi > +\Delta \end{cases} . \tag{6}$$

For the solid body with simple boundary, the LS function ϕ can be obtained according to its definition directly with the explicit expression for boundary surface. For example, for the circular cylinder, ϕ can be defined by $\phi = D_{x,c} - r_c$, where $D_{x,c}$ denotes the distance from a given grid point to the centre of the cylinder and r_c denotes the radius of the cylinder. For the cases with rigid structure undergoing both translational and rotational motions, the local coordinates to the body centre $x_{l,c} = \boldsymbol{T} \cdot (x - x_c)$ is used to update ϕ, where $\boldsymbol{T}$ is defined as $\boldsymbol{T}_{i,j} = \boldsymbol{e}_{i,j}$ and $\boldsymbol{e}_{i,j}$ denotes the components of the base vectors fixed on the rigid body, as shown in Fig. 2(a).

For the solid body with complex boundary, an efficient reconstruction algorithm based on the concept of bounding box and the pseudonormal has been developed to obtain and to update the LS function ϕ. As shown in Fig. 2(b), normal vectors are firstly obtained on the line segments and vertices of the boundary surface. The edge normal is defined in its usual way, while the vertex normal is defined by the average of the corresponding two edge normals. To update ϕ, traverse about the line segments is carried out. For each boundary edge, a bounding box consisting of Euler grid nodes is built firstly, as shown in Fig. 2(b) (the width of the bounding box relates to the scale of the segment and the width of the diffused interface Δ). For each Euler point inside the bounding box, the nearest point (projection point) on the edge and the absolute distance $|\phi|$ can be obtained easily. When such projection point is on the edge, the product between the vector from projection point to the Euler point and the edge normal is used to determine the sign of ϕ, while the vertex normal is used to obtain such ± 1 sign, when the projection point coincides with the vertex, which are the cases for A and B in Fig. 2(b) respectively. When the Euler point is accessed multiple times by different boundary segments (C in Fig. 2(b)), its ϕ value is defined with that with smaller $|\phi|$. With such algorithm, ϕ can be reconstructed with complexity of $O(N_S)$ in a narrow band around the solid boundary, where N_S denotes the amount of surface segments to represent the body surface. The remaining ϕ values on the Euler nodes can be defined with the maximum positive and minimum negative ϕ values during the boundary segment traverse. It should be mentioned that even line segments are essential to reconstruct ϕ, its density only affects the representation of the surface boundary, while has no direct effect on the flow prediction. For the solid boundary with sharp corners, local refinement is essential for its accurate presentation. The further details about the bounding box based reconstruction algorithm for ϕ can be found in Baerentzen and Aanaes (2005) and Liu and Hu (2014).

3.1 VOS model for the field extension

Strictly speaking, the NS equations and the LBE are defined in the fluid domain only. The key concept of the VOS based IB model is to extend the equations to the solid phase to form a unified equation that can be applied in the whole domain. For the rigid body, the velocity is well-defined in the solid phase. Therefore, a natural strategy for equation reconstruction is the weighted average of the flow equations and the solid motion. Taking the NS equations as an example, the following equations are defined in the whole domain,
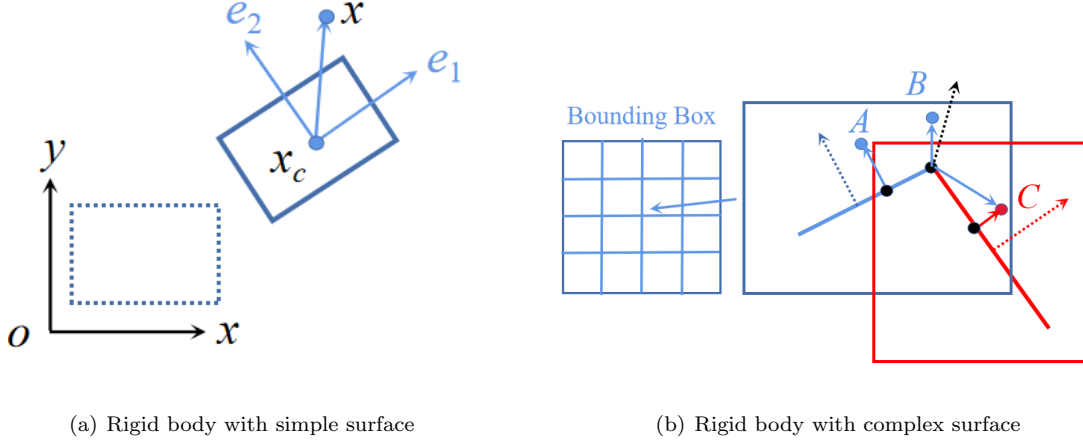
(a) Rigid body with simple surface   (b) Rigid body with complex surface

Fig. 2. Numerical strategy for the definition of LS function.

$$(1 - \alpha)\left[U_t + (U \cdot \nabla)U + \frac{1}{\rho_f}\nabla P - \nu\nabla^2 U \right] + \alpha(U - U_s)/\delta t = 0,$$

$$\nabla \cdot U = 0, \tag{7}$$

where δt denotes the time increment and is adopted to achieve the dimension balancing, and U_s is the target velocity determined by the body motion. It can be observed that those equations tend to be the NS equations in the fluid domain and the solid velocity can be recovered in the solid domain. If the pressure can be defined properly, by using the explicit Euler scheme for the flow prediction, the velocity can be obtained as

$$U^{n+1} = \alpha U_s + (1 - \alpha)\tilde{U}, \tag{8}$$

where $\tilde{U} = U^n + N(U^n, P)\delta t$ denotes the velocity without the effect of solid phase and $N(U^n, P)$ represents the contribution from the convection term, diffusion term and pressure gradients to the momentum of the fluid flow. As it can be seen, the velocity varies smoothly in the whole domain, therefore, the no-slip condition is implicitly enforced without any special treatment.

As shown in Eq. (7), the flow equation takes different forms in the fluid and solid phases. By rearranging, Eq. (7) can be reformulated as

$$U_t + (U \cdot \nabla)U + \frac{1}{\rho_f}\nabla P - \nu\nabla^2 U = \alpha\left[(U_s - U)/\delta t + U_t + (U \cdot \nabla)U + \frac{1}{\rho_f}\nabla P - \nu\nabla^2 U \right],$$

$$\nabla \cdot U = 0. \tag{9}$$

It is obvious that the LHS of the equation is the same as the normal NS equations for fluid phase, which is consistent in the whole domain. On the RHS of the equation, it vanishes in the fluid phase and transits smoothly to the solid phase. By denoting such term as a forcing term, the NS equations can be reformulated as

$$U_t + (U \cdot \nabla)U + \frac{1}{\rho_f}\nabla P - \nu\nabla^2 U = \alpha f,$$

$$\nabla \cdot U = 0, \tag{10}$$

where f relates to the solid velocity and is implicitly defined to enforce the motion of rigid body. Eqs. (7) and (10) demonstrate that the effect of the solid body on the fluid flow is equivalent to adding a forcing term to the solid phase.

For the LBM, the field extension is not as obvious as the above formulation because the flow field is defined with the distribution function, rather than the macro-scale velocity and pressure. Therefore, a modified formulation should be built firstly to achieve the extension of LBE. In the solid phase, the solid velocity can be enforced by $q_\alpha = q_\alpha^s = q_\alpha^{s,eq}(U_s) + q_\alpha^{s,neq}$, where q_α^s is the solid distribution function, $q_\alpha^{s,eq}$ its equilibrium state and $q_\alpha^{s,neq}$ its non-equilibrium part. In the definition of q_α^s, the macro-scale behaviour is defined by its equilibrium part only, while the remaining non-equilibrium part makes no contribution to the velocity field and is implicitly defined. With the solid distribution function, the distribution function inside the solid domain follows

$$q_\alpha - q_\alpha^s = 0. \tag{11}$$

In the fluid domain, the evolution of the distribution function follows the LBE defined in Eq. (3), while the behaviour of the distribution functions should follow Eq. (11) to reproduce the rigid motion inside the solid domain. As it has been investigated in Weymouth and Yue (2011), the convolution of Eqs. (3) and (11) with Heaviside function is an efficient way to couple the flow behaviour and rigid motion of solid body. Similar to Eq. (7), adopting the first-order approximation of their convolution term (Weymouth and Yue, 2011), a unified equation for the evolution of the distribution function can be obtained as

$$(1 - \alpha)\left[q_\alpha(x + e_\alpha\delta t, t + \delta t) - q_\alpha(x,t) - \Omega_\alpha(x,t)\right] + \alpha\left[q_\alpha(x + e_\alpha\delta t, t + \delta t) - q_\alpha^s(x + e_\alpha\delta t, t + \delta t)\right] = 0. \tag{12}$$

In this way, the LBE can be extended to the whole domain.

3.2 VOS based Immersed Boundary method for LBM

Different from macro-scale NS solvers, the LB solver adopts the distribution function to describe the fluid flow. To implement the direct forcing model in the framework of LBM, similar with the strategy to obtain Eq. (10), Eq. (12) can be reformulated as

$$\begin{aligned}
&q_\alpha(x + e_\alpha\delta t, t + \delta t) - q_\alpha(x,t) - \Omega_\alpha(x,t) \\
=&\alpha\left[q_\alpha^s(x + e_\alpha\delta t, t + \delta t) - q_\alpha(x + e_\alpha\delta t, t + \delta t) + q_\alpha(x + e_\alpha\delta t, t + \delta t) - q_\alpha(x,t) - \Omega_\alpha(x,t)\right] \\
=&\alpha\left[q_\alpha^s(x + e_\alpha\delta t, t + \delta t) - q_\alpha^*(x,t)\right],
\end{aligned} \tag{13}$$

where $q_\alpha^* = q_\alpha + \Omega_\alpha$ denotes the post-collision distribution function.

Following Eq. (10), the RHS of Eq. (13) is modelled as an implicitly defined forcing term F_α. As it can be observed, Eq. (13) shows obvious implicit characteristics. To remove such implicitness, $q_\alpha^s(x + e_\alpha\delta t, t + \delta t)$ is evaluated at (x,t), rather than $(x + e_\alpha\delta t, t + \delta t)$, and such treatment is equivalent to split Eq. (13) into the separated collision-streaming processes,

$$\tilde{q}_\alpha(x,t) = (1-\alpha)q_\alpha^*(x,t) + \alpha q_\alpha^s(x,t) = q_\alpha^*(x,t) + \alpha F_\alpha \tag{14}$$

$$q_\alpha(x + e_\alpha \delta t, t + \delta t) = \tilde{q}_\alpha(x,t).$$

In Eq. (14), the effect of the forcing term F_α is to drive the distribution to its solid state, which is an analogy to the effect of body force in Eq. (10). As it can be observed, the effect of such forcing term is equivalent to the body force in the macro-scale. Therefore, to conserve the mass in the whole domain, the F_α term is selected as the forcing term with the macro-scale body force. To cancel the inconsistent velocity, the body force should follow

$$f = \beta \frac{U_s - U^n}{\delta t}. \tag{15}$$

In the previous works (Wu and Shu, 2009; Kang and Hassan, 2011; Favier et al., 2014), β has been set to 2.0 to match the equilibrium fluid velocity $U^{eq} = \sum_\alpha f_\alpha e_\alpha / \rho_f + \frac{1}{2}f\delta t$ to its target value, which is fairly good for the surface based direct forcing model. However, with such forcing strategy, even the contribution from the forcing term to U^{eq} is $\frac{1}{2}f\delta t$, the remaining contribution to the post-collision distribution function and the resultant velocity is also $\frac{1}{2}f\delta t$. Taking a fixed cylinder in uniform flow as a simple example, the initial condition is often set as $U = (U_\infty, 0)$ in the whole domain. Therefore, the forcing term should drive the distribution function to $\boldsymbol{Q}^s(U_s = 0)$. With $f = 2\frac{U_s - U^n}{\delta t}$, U^{eq} is well enforced. However, considering the post-collision state with such forcing term, the flow velocity in the solid domain will be driven to $U = (-U_\infty, 0)$. It is an obvious over-correction about the fluid velocity in the solid phase. As it will be shown later, this inconsistency leads to serious force oscillations during the initial stage of the simulation and such unphysical phenomenon lasts for a long time. The present work suggests that $\beta = 1.0$ can properly drive the distribution function and further the fluid velocity to their target states. For the fixed cylinder, even the corrected equilibrium velocity is $0.5U_\infty$, the remaining contribution from the forcing term leads to the recovery of static state in the solid phase. After the collision stage with such forcing term, the velocity can be driven to 0.0 as expected. In this way, at least in the sense of numerical experiments, the force oscillation can be well controlled.

To account for the forcing term effects on the distribution functions, the model in Guo et al. (2002) is adopted. The overall algorithm of the present IB-LBM model can be summarised as Algorithm 1.

3.3 Indirect method for the force prediction

To obtain the hydrodynamic force on the structure, an indirect method without surface integral is developed in the present work. Considering the definition of the hydrodynamic force on the structure

$$\mathbf{F} = \int_{\partial S} \boldsymbol{\sigma} \cdot \mathbf{n} dS,$$
$$\mathbf{M} = \int_{\partial S} \mathbf{r}_s \times (\boldsymbol{\sigma} \cdot \mathbf{n}) dS, \tag{16}$$

where ∂S denotes the surface of the structure, $\mathbf{r}_s$ is the location of the surface grid point relative to its mass centre, $\boldsymbol{n}$ is the unit normal vector on the surface grid point, and $\boldsymbol{\sigma} = -P\mathbf{I} + \boldsymbol{\tau}$ is the stress tensor. To evaluate

---
Algorithm 1: IB-LBM algorithm
---
(1) The distribution functions are well-defined at $t = t^n$.

(2) Define the macro-scale flow field with the distribution functions,

$$\rho_f = \sum_\alpha q_\alpha, \quad \hat{U} = \sum_\alpha q_\alpha e_\alpha / \rho_f.$$

(3) Define the LS function ϕ, with analytical expression based on local coordinates for rigid body with simple boundary or bounding box based reconstruction algorithm for rigid body with complex boundary.

(4) Define the VOS function α with Eq. (6).

(5) Obtain the forcing term with the direct forcing model,

$$f = \beta \frac{U_s - \hat{U}}{\delta t}.$$

(6) Loading evaluation based on the indirect force prediction model.

(7) For cases with Fluid-Structure Interaction, update the location and motion of rigid body.

(8) With the forcing term, advance the flow field using the algorithm in Eq. (14).

(9) $n = n + 1$, return to (1).
---

the force on the structure using Eq. (16), interpolation is essential to obtain the stress tensor on the surface Lagrangian points, which may not coincide with the Euler points. To avoid such interpolation, the surface integral is transformed into the volume integral with the Green's theorem. To achieve such goal, Eq. (16) is firstly transformed into its general form according to the principle of virtual work

$$\sum_i \hat{F}_i \delta\xi_i = \sum_i \int_{\partial S} \delta\mathbf{r}_{s,i} \cdot (\boldsymbol{\sigma} \cdot \mathbf{n}) dS, \tag{17}$$

where $\hat{F}_i$ denotes the general force component and $\delta\mathbf{r}_{s,i}$ is the virtual boundary displacement under general virtual displacement on the mass centre of the structure $\delta\xi_i$. In the definition of force components, $i = 1 - 3$ denotes the translational mode and $i = 4 - 6$ denotes the rotational mode for 3D cases, while $i = 1 - 2$ denotes the translational mode and $i = 3$ denotes the rotational mode for 2D cases. Considering the arbitrary value of $\delta\xi_i$, with the Green's theorem, the force component $\hat{F}_i$ can be written as

$$\hat{F}_i = \int_S (\nabla \delta\tilde{\mathbf{r}}_{s,i}) : \boldsymbol{\sigma} dV + \int_S \delta\tilde{\mathbf{r}}_{s,i} \cdot (\nabla \cdot \boldsymbol{\sigma}) dV, \tag{18}$$

where $\delta\tilde{\mathbf{r}}_{s,i}$ is defined as $\delta\mathbf{r}_{s,i} = \delta\xi_i \delta\tilde{\mathbf{r}}_{s,i}$ (no summation about i), and denotes the unit virtual boundary displacement in mode i.

Within the present volume based IB framework, consistent velocity correction has been carried out in the whole solid phase. Therefore, in the solid domain S, strain tensor can be evaluated by the rigid velocity, $\varepsilon_{ij} = \frac{1}{2}(u_{s,i,j} + u_{s,j,i})$, with an error $O(\delta t)$ at a conservative estimate. For the rigid body motion, the rigid velocity is strain-free ($\varepsilon_{ij} = 0$), and such characteristic leads to the vanishing of viscous stress, i.e., $\tau_{ij} = 2\rho_f \nu \varepsilon_{ij} = 0$. Therefore, the first term in Eq. (18) can be evaluated by $(\nabla \delta\tilde{\mathbf{r}}_{s,i}) : \boldsymbol{\sigma} = -P(\nabla \cdot \delta\tilde{\mathbf{r}}_{s,i})$. In addition, as $\nabla \cdot \delta\tilde{\mathbf{r}}_{s,i} = 0$ for the rigid body motion (divergence-free condition for the rigid motion), the contribution from the first term

in Eq. (18) equals 0. Within the transition region around the boundary surface, the divergence-free condition still holds, but the viscous stress appears, because of the smooth transition of rigid velocity to flow velocity. Therefore, extra error exists for the force prediction with the present indirect model. Because the width of the transition region is comparable with grid spacing, it is believed that such contribution is $\Delta \hat{F}_i = O(\delta x)$ at a conservative estimate. Using Eq. (10), the second term in Eq. (18) can be further simplified as

$$
\begin{aligned}
\hat{F}_i &= \int_S \delta \tilde{\mathbf{r}}_{s,i} \cdot \rho_f \left[U_t + (U \cdot \nabla)U - \alpha f \right] dV \\
&= \int_S \delta \tilde{\mathbf{r}}_{s,i} \cdot \rho_f \left(\frac{DU}{Dt} - \alpha f \right) dV = \int_S \delta \tilde{\mathbf{r}}_{s,i} \cdot \left(\rho_f \frac{DU}{Dt} \right) dV + \int_S \delta \tilde{\mathbf{r}}_{s,i} \cdot (-\alpha \rho_f f) dV.
\end{aligned}
\tag{19}
$$

Eq. (19) indicates that the hydrodynamic force under the rigid body mode can be evaluated as the integral of the IB force and the negative inertial force inside the solid domain without the need of the integral about flow stress over the body surface. In Suzuki and Inamuro (2011), Eq. (19) was proved. For the rotational modes, Suzuki and Inamuro (2011) introduced the extra Lagrangian points to evaluate the inertial momentum of the fluid flow. The reason for such strategy is that for the surface based IB model, the forcing term is only applied on the surface of the structure. Therefore, the internal flow shows difference with the solid motion. In the present model, because of the enforcement of rigid body motion for the entire solid phase, the rigid body motion can be well-enforced and the first term in the RHS of Eq. (19) can be further simplified for all the rigid body modes (rigid body assumption). Compared with the work in Suzuki and Inamuro (2011), no extra Lagrangian points are needed and the algorithm for the internal momentum evaluation is simplified, which further improves the efficiency of the present model.

As it has been discussed in Eq. (19), for the rigid body, the force prediction can be simplified considerably (the integral of fluid acceleration term can be evaluated by the inertial mass and moment of the body filled with fluid), which is the case of the present work. For the flexible body with arbitrary deformation, such force prediction model relates to the evaluation of fluid acceleration at a certain Euler grid point, which may not be coincident with the structure grid. Furthermore, for the flexible body, the divergence and strain of the velocity field inside the solid domain lead to extra corrections about the force prediction, as shown in Eq. (18). Generally speaking, the present version of the IB-LBM model can be only applied to the interaction between rigid body and fluid flow, while for the general flexible structure, a robust interpolation model to transfer the body response from structure grid to Euler grid is essential and it is one of our research topics in the future.

4 Numerical Results

In the previous sections, the present VOS based IB algorithm in the framework of direct forcing model has been developed and coupled with LBM to solve the fluid-body interactions. To validate the accuracy and the robustness of the present model, in this section, numerical simulations are carried out for the interaction between fluid flows and solid bodies, which include the structures with both simple and complex boundaries. In the present work, the Reynolds number covers the low to moderate region, i.e. $Re = O(10^1) - O(10^3)$. Therefore, no turbulence model is activated during the simulation.

4.1 Steady flow around a fixed cylinder

In this subsection, steady flow around a fixed cylinder is simulated to confirm the performance of the present VOS based IB strategy to enforce the no-slip boundary condition on the surface of the structure. With such configuration about fluid flow and solid body, the only parametre affecting the flow pattern is Reynolds number $Re = \frac{U_\infty D}{\nu}$, where U_∞ and D denote the inlet velocity of the fluid flow and the diametre of the cylinder respectively.

With $Re = 5 - 40$, steady flow can be observed around the cylinder. As shown in Fig. 3, with $Re = 40$, a pair of steady re-attached region exists around the cylinder. As it has been observed in Coutanceau and Bouard (1977) and numerically simulated by Berthelsen and Faltinsen (2008), flow seperation occurs at $\theta \approx 53° - 54°$. Adopting present VOS based IB model, as it can be observed in Fig. 3(a), the prediction about the location of seperation matches well with the previous ones. Furthermore, compared with the flow pattern adopting surface based direct forcing model(Figs. 3(b) and 3(c)), the flow penetration has been weakened considerably and the unphysical flow within the solid domain has been controlled. With the present IB strategy, the forcing term to enforce the solid body motion is evaluated in an explicit manner, and implicit forcing term iteration, which has been adopted in Wu and Shu (2009) and Zhao et al. (2021), is avoided. Such treatment leads to the efficiency of the present IB algorithm.

As shown in Fig. 4, discontinuity can be observed for the pressure prediction with the surface based direct forcing model. Despite of its limited effect on the pressure prediction in the fluid domain as shown in Fig. 4 for the fixed structure, the evaluation of hydrodynamic force on the moving structure can be affected and special attention should be paid to remedy such issue. With the present IB model, because of the consistent velocity correction for the solid phase, a smooth pressure field can be obtained and such phenomenon is helpful for the force prediction about moving structure.

4.2 Unsteady flow around an oscillating cylinder

In this subsection, the unsteady flow around an oscillating cylinder is simulated to confirm the performance of the present IB model for moving boundary cases. According to the work in Dutsch et al. (1998), the cylinder is forced to oscillate horizontally with a prescribed amplitude A_{max} and frequency f. In this case, Re is defined based on the maximum velocity $U_{max} = 2\pi f A_{max}$ and the Keulegan-Carpenter number KC is defined as $KC = \frac{U_{max}}{fD}$, where D denotes the diameter of the cylinder. As reported in Dutsch et al. (1998), when $KC = 5$ and $Re = 100$, a stable periodic flow pattern and force history can be obtained. Considering the characteristic of stability, this case is selected in the present work as the benchmark. As shown in Fig. 5, convergence test has been carried out firstly to check the numerical performance of the present algorithm. In this case, a coarse grid with $D = 12.5\delta x$ has been adopted as the base grid, and the grid has been refined to $L = 2 - 4$ to reach the desirable resolution. During the simulation, a constant $Ma \approx 0.1$ has been enforced by keeping a constant $\delta t = \frac{T}{1000}$ on the base grid. As it can be observed, with $D = 100\delta x$, convergence has been reached and further grid refinement makes no obvious improvement about force prediction.

The force coefficients C_ds obtained with different β values and IB strategies are shown in Fig. 6. As it can be observed in Fig. 6(a), with $\beta = 2.0$, according to the relating discussion in Section 3.2, the over-correction about the velocity in the solid phase induces a long-term unphysical force oscillation. For the present case, the unphysical oscillation decays in an exponential manner. Furthermore, with the decaying of force oscillation,
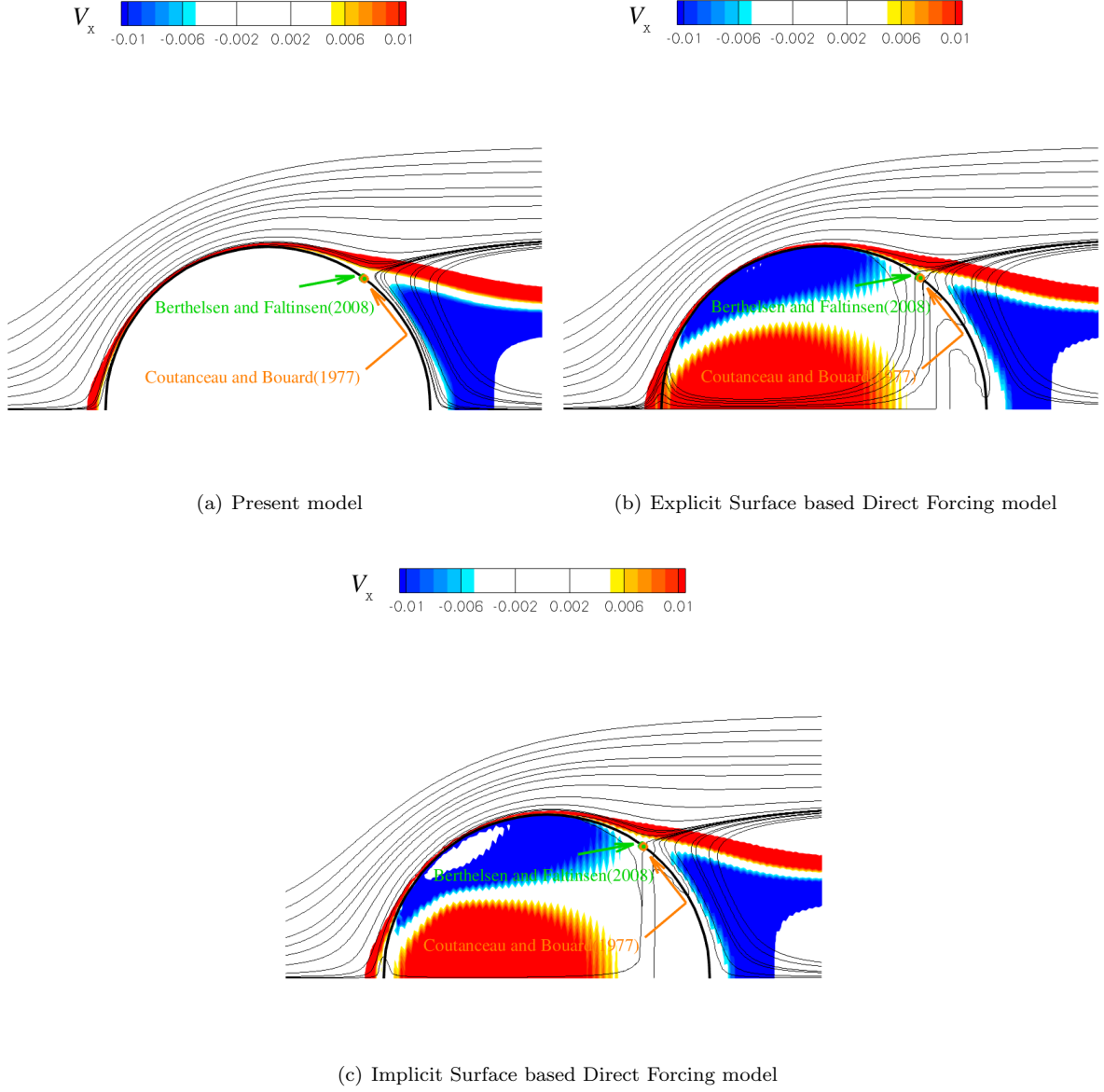
(a) Present model

(b) Explicit Surface based Direct Forcing model

(c) Implicit Surface based Direct Forcing model

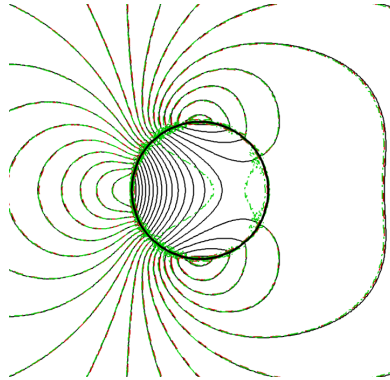**Fig. 3.** Steady flow around a fixed cylinder with $Re = 40$.

Fig. 4. Pressure Contours with $Re = 40$, where black solid, red dashed and green dash-dotted lines denote contours with present VOS based IB model, explicit surface based and implicit surface based direct forcing model respectively.

the force predictions with different β values match well with each other ($4.0 \leq t/T \leq 5.0$ in Fig. 6(a)). Meanwhile, the reliability of the present forcing factor $\beta = 1.0$ is confirmed, and the horizontal force reaches its stable periodic state after a transition stage around $t = 1.0T$ (Fig. 6(b)). In addition, even with the velocity correction around the solid boundary only, i.e., the surface based direct forcing model, the force oscillation cannot be completely removed during the initial stage before $t = 2.0T$. As shown in Fig. 6(b), the present VOS based direct forcing model performs well, without any visible oscillation even at the beginning of the simulation. With the evolution of the cylinder oscillation, the unphysical force oscillation vanishes and the force predictions with all the mentioned IB strategies match each other well and are in good agreement with the previous results in Dutsch et al. (1998), as shown in Fig. 7. In Fig. 8, with the present KC and Re numbers, the symmetrical flow field around the cylinder can be observed and the flow pattern matches well with that in Dutsch et al. (1998).
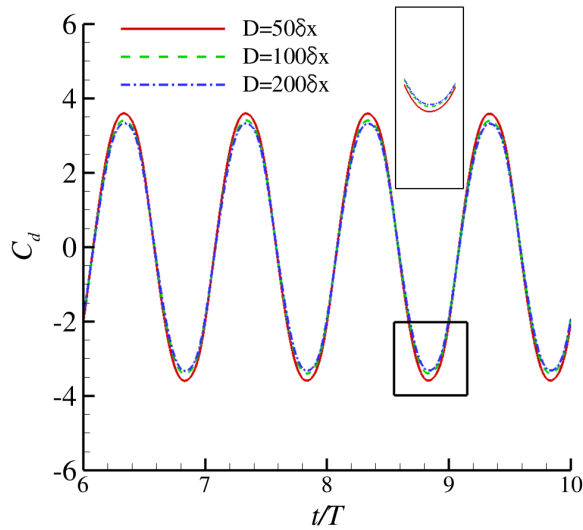
Fig. 5. Convergence test about the hydrodynamic force on the oscillating cylinder with $KC = 5$ and $Re = 100$.

4.3 Unsteady flow around a hovering wing

In this subsection, the unsteady flow caused by a hovering wing undergoing a forced periodic motion along a straight line in the stationary fluid is simulated. The thin elliptical wing with the aspect ratio of $w/c = 0.25$, where c denotes the chord length and w is the thickness of the wing, is adopted. The translational motion of the centre of the wing follows
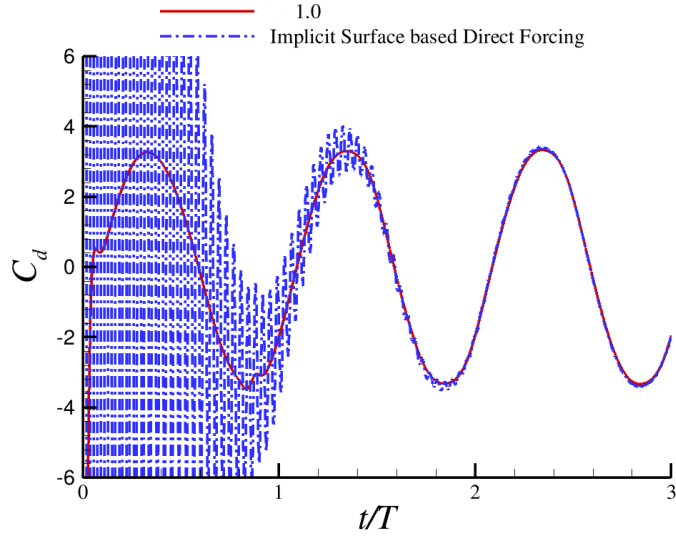
$$x = \frac{A_0}{2} \cos\left(\frac{2\pi t}{T}\right) \cos\beta, \quad y = \frac{A_0}{2} \cos\left(\frac{2\pi t}{T}\right) \sin\beta. \tag{20}$$

In addition to the translational motion, the wing also experiences the rotational motion about its centre which is enforced by

$$\alpha = \frac{\pi}{4}\left[1 - \sin\left(\frac{2\pi t}{T} + \phi\right)\right]. \tag{21}$$

15
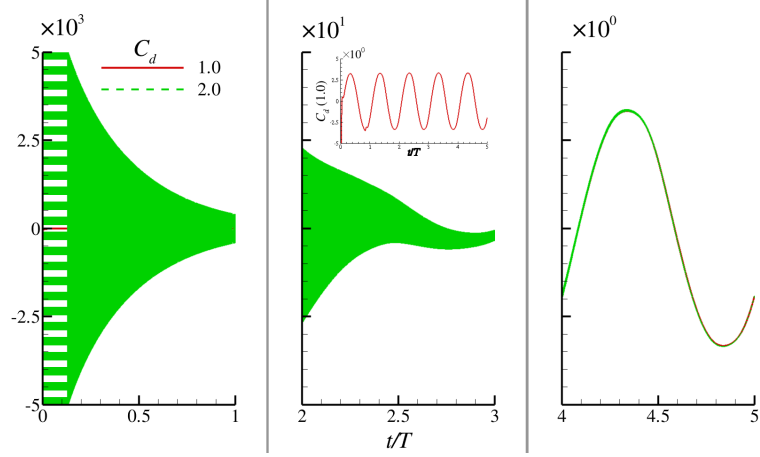
(a) Different β values

(b) Surface based and volume based strategies

Fig. 6. Hydrodynamic force on the oscillating cylinder with $KC = 5$ and $Re = 100$ during the initial stage.
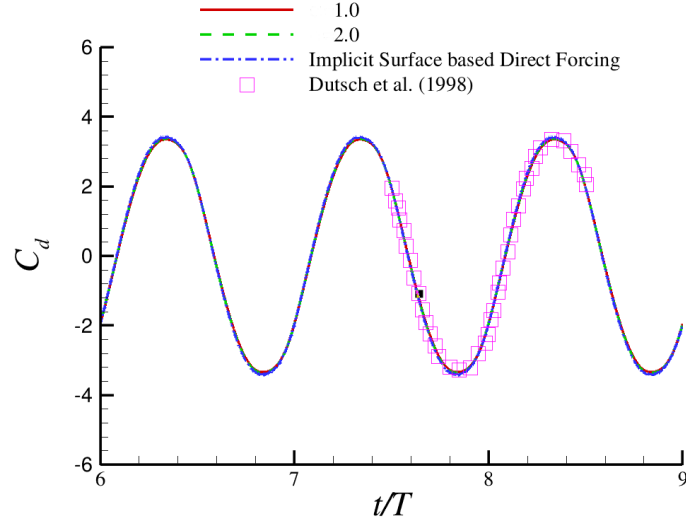
Fig. 7. Comparison of the hydrodynamic force on the oscillating cylinder with $KC = 5$ and $Re = 100$ during the steady stage with the previous results in Dutsch et al. (1998).
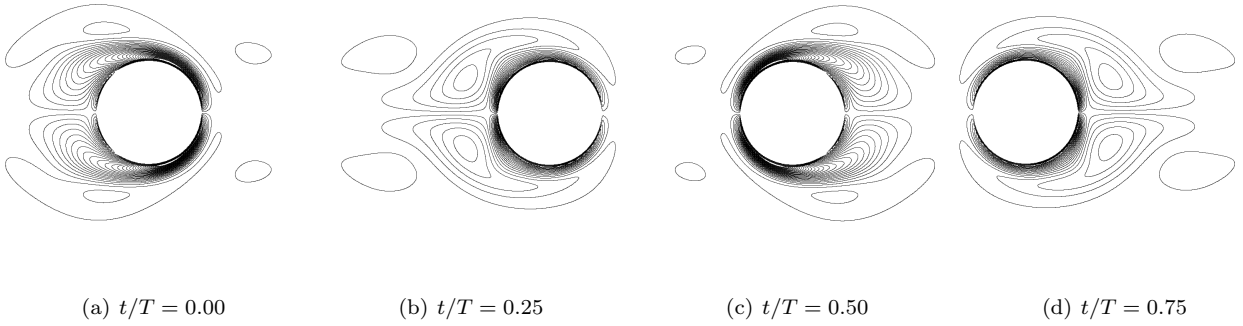

(a) $t/T = 0.00$ (b) $t/T = 0.25$ (c) $t/T = 0.50$ (d) $t/T = 0.75$

Fig. 8. Flow field around the oscillating cylinder with $KC = 5$ and $Re = 100$ at different time instants.

In the present simulation, the same parameters as that in Xu and Wang (2006), i.e., $A_0/c = 2.5$, $\beta = \pi/3$, $\phi = 0.0$ and $Re = 157$, are adopted with c as the length scale and $\pi A_0/T$ as the velocity scale, where T denotes the flapping period. It should be mentioned that, compared with the definition in Xu and Wang (2006), the mean location of the wing centre here is shifted to $x = 0$ and $y = 0$, which has no effect on the force calculation and flow prediction.

As shown in Fig. 9, the present results about the forces on the wing match well with the previous ones in Xu and Wang (2006) and Yang and Stern (2012). Furthermore, the flow fields around the wing within one flapping cycle are shown in Fig. 10. At the beginning of the downward stroke, a strong positive vortex caused by the clockwise rotation of the wing around the tip-A can be observed. Due to the counter-clockwise rotation of the wing, a negative vortex is formed on the opposite side of the wing and the previous vortex travels to the tip-B and is enhanced by the motion of the wing. With the wing moving further, the dettachment of the positive vortex occurs, and the negative vortex moves to the tip-B. As shown in Fig. 10(c), when the rotation direction of the wing changes, the negative vortex re-attaches to the wing and couples with the positive vortex to form a vortex dipole. Such behaviour can be traced back to the non-zero mean angle of the rotational motion.
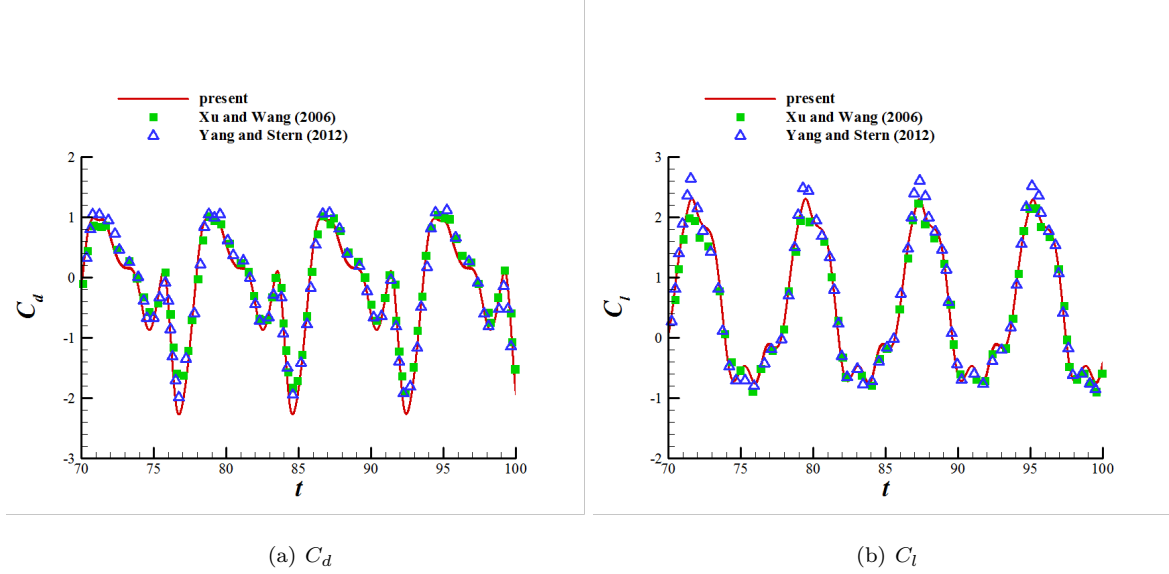

(a) C_d

(b) C_l

Fig. 9. Hydrodynamic forces on the hovering wing at $Re = 157$ and the comparison with the previous results.

(a) $t = \frac{0}{5}T$ (b) $t = \frac{1}{5}T$ (c) $t = \frac{2}{5}T$ (d) $t = \frac{3}{5}T$ (e) $t = \frac{4}{5}T$
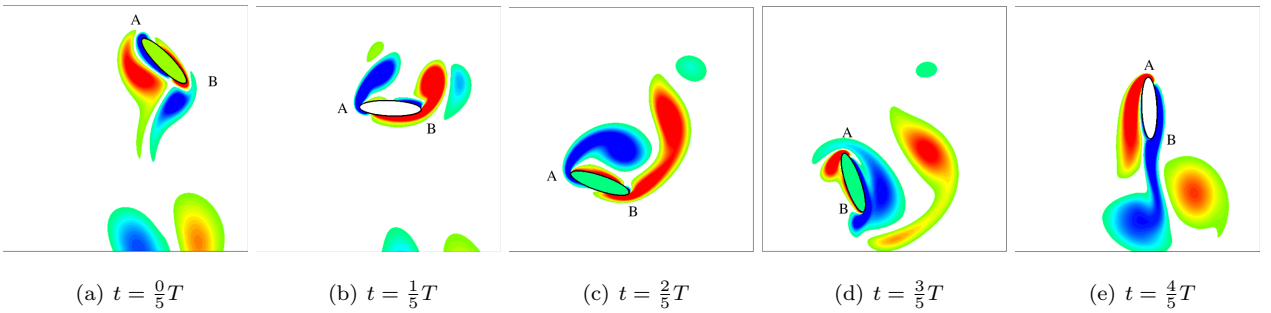
Fig. 10. Flow field around the hovering wing at $Re = 157$.

4.4 Unsteady flow around a complex C-shape body

To show the performance of the present model to predict the fluid flow caused by rigid body with complex boundary, in this subsection, the unsteady flow caused by a C-shape rigid structure is carried out. As shown in Fig. 11, the C-shape body consists four sets of semicircles. With the present configuration, Re is defined with D and U_∞ as the length scale and velocity scale. Similar with the numerical simulation with a Diffused Vortex Hydrodynamics (DVH) model (Rossi et al., 2015), $Re = 2000$ is adopted here with $0 \leq \alpha \leq \frac{\pi}{2}$. As it has been shown in Rossi et al. (2015), with the increase of α from $\alpha = 0$, the case where the fluid flow shows periodical characteristics, the regularity of hydrodynamic loading on the body is firstly lost. With a further increase of α from a certain value, restoring of periodical behaviour of the fluid flow can be observed again. With $\alpha = \frac{\pi}{2}$, the loading on the structure becomes almost periodical.

In this subsection, our main goal is to check the performance of the present IB-LBM algorithm for cases with complex boundaries, therefore, only qualitative computations are carried out for various αs. As it can be observed in Fig. 12, the predictions about hydrodynamic loading on the structure match well with that obtained with DVH model (it should be mentioned that, to accelarate the process reaching its possible periodical state, disturbance has been added to the motion of the body, and the original data from Rossi et al. (2015) has been shifted to match the phase difference between the present results and previous ones). The mean drag coefficient and the amplitude of lift coefficient increase with α. Specially, with $\alpha = 0$, the cavity flow trapped in the lower region of the C-shape body (Fig. 13(a)) leads to the formation of low pressure region and further results the negative mean lift force on the body. From the viewpoint of flow structure, with $\alpha = 0$, the upper part of the vortex flow matches well with that of the circular cylinder, and because of the mentioned cavity flow, the fluid beneath the C-section pass the rigid body as if there is no hole, i.e., D-shape cylinder with identical orientation. For $\alpha = \frac{\pi}{2}$ case, the overall far field wake pattern is similar with that of the full cylinder. While in the near field of the C-section, the dettached vortex is firstly trapped inside the hole with the action of the former vortex. Different from that with $\alpha = 0$, the cavity flow with such configuration is unsteady. The existence of the hole leads to the complex interaction between the dettached vortex and the rigid boundary (Fig. 13(c)), and such interaction is believed to be one of the main sources for the formation of weak irregularity of hydrodynamic loading on the structure, as shown in Fig. 12. With the dettachment of vortex into the wake flow, the trapped vortex in the cavity escapes and leads to the formation of Karman vortex street. With $\alpha = \frac{\pi}{4}$, the flow pattern is rather complex, featured by the vortex mergence and splitting. With such vortex-vortex and vortex-structure interactions, irregular hydrodynamic loading can be observed on the structure, which is consistent with the results by Rossi et al. (2015). Even the bifurcation behaviour of the fluid flow passing the C-shape body is interesting and worth investigation in detail, such work is beyond the goal of the present work and it will be one of our research topics in the future. As it has been presented, both the qualitative and quantitative results in this subsection show the capacity of the present IB-LBM model to treat fluid flow relating to complex boundaries.

4.5 Unsteady flow around a pitching foil

To validate the present model for the thin-wall structure with moving boundary, the hydrodynamic performance of a pitching foil is tested. Firstly, numerical simulation about a pitching foil at $Re = 500$ is carried out to check the performance of the present model with relatively low Re numbers. In this part, two sets of
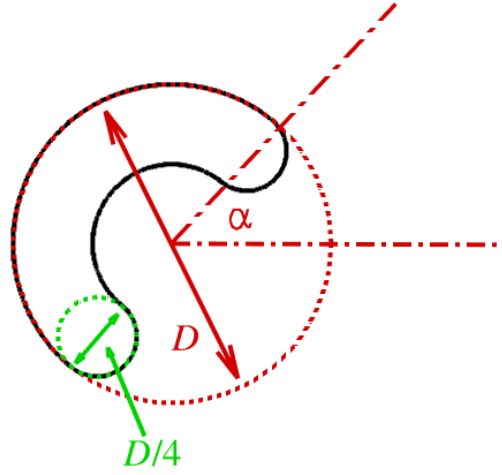
19

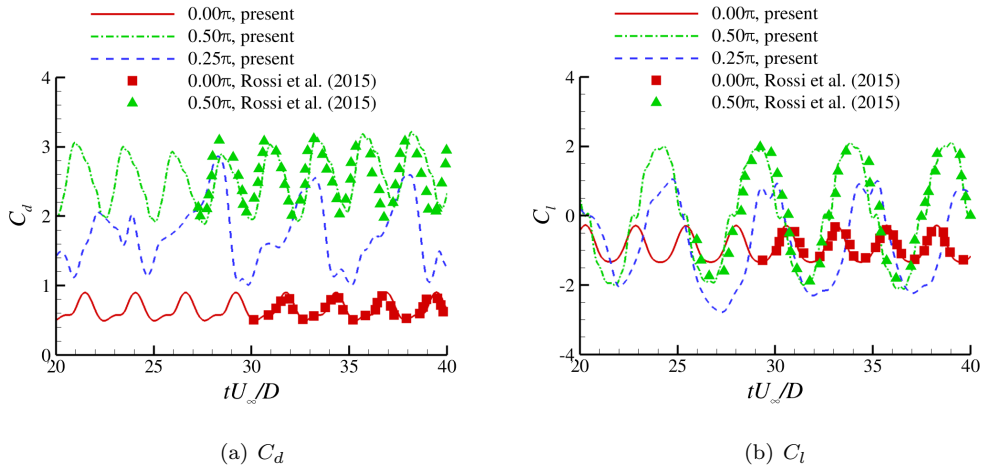**Fig. 11.** Sketch diagram of the C-shape body with an Angle of Attack (AoA) α.

(a) C_d

(b) C_l

Fig. 12. Hydrodynamic forces on the C-shape body with $Re = 2000$.

(a) $\alpha = 0$ at $tU_\infty/D = 37.5$

(b) $\alpha = \frac{\pi}{4}$ at $tU_\infty/D = 38.0$
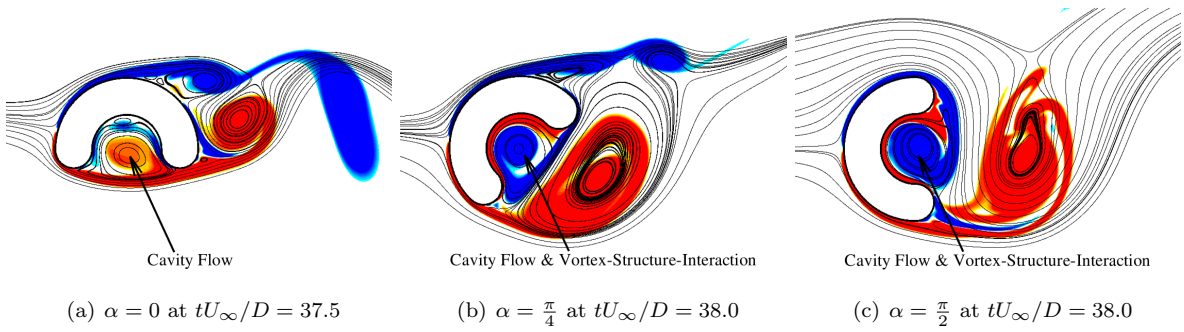
(c) $\alpha = \frac{\pi}{2}$ at $tU_\infty/D = 38.0$

Fig. 13. Flow field around the C-shape body with $Re = 2000$.

Strouhal numbers St, i.e., $St = 0.2$ and $St = 0.4$, which are defined by the motion amplitude of the foil tip in the y direction, are adopted. In Senturk and Smits (2018), a thin plate without thickness has been adopted. With the present IB strategy, such a thin-wall structure should be modelled with an artificial thickness with few grid spacing. In the present cases, an artificial thickness of the foil $t/L = 2\%$ has been adopted. As shown in Fig. 14, both the thrust and the lift coefficients of the foil predicted by the present model match well with the previous results (Senturk and Smits, 2018). At $St = 0.2$, a negative mean thrust is observed, which is the result of the normal vortex street in the wake of the foil shown in Fig. 15(a). In this case, because of the relatively small St number, the stability of the symmetrical wake is preserved and the resulting thrust and lift on the foil are symmetrical. With the increase of St to $St = 0.4$, the trailing edge vortex (TEV) is enhanced as shown in Fig. 15(b). Other than the enhanced TEV, the leading edge vortex (LEV) becomes obvious and the complex behaviours of the LEV can be observed. The enhanced TEV leads to the symmetric breaking of the wake flow and a vortex dipole can be observed. In this case, the wake flow leans to one side of the foil.
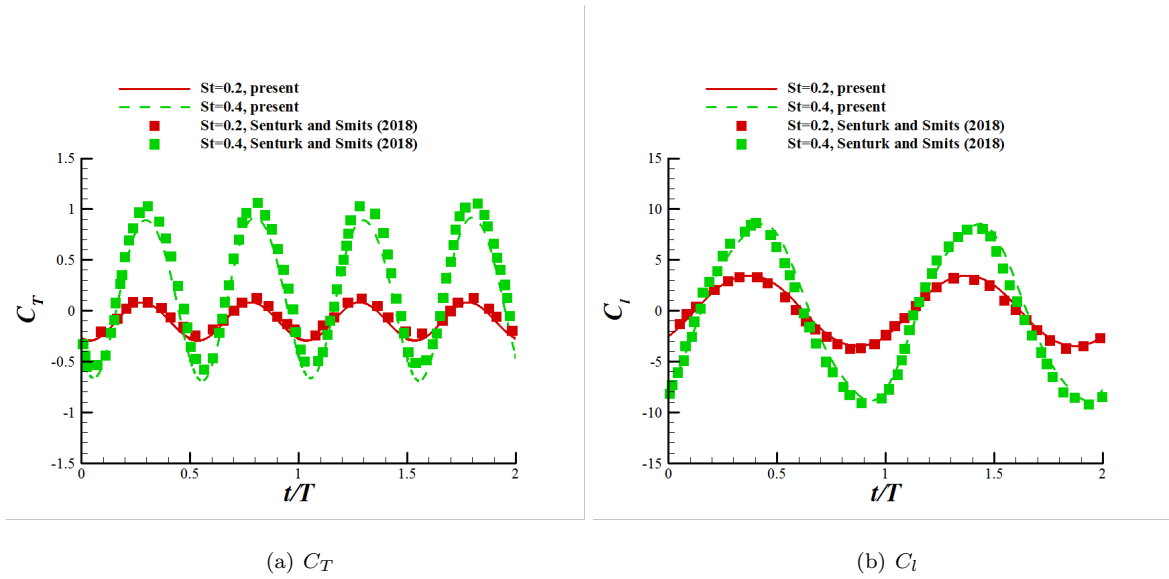

(a) C_T

(b) C_l

Fig. 14. Hydrodynamic performance of the pitching plate at $Re = 500$.
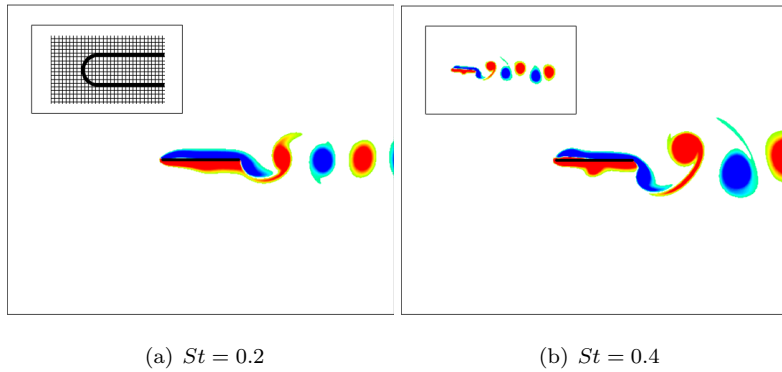

(a) $St = 0.2$

(b) $St = 0.4$

Fig. 15. Wake flow of the pitching plate at $Re = 500$.

Further, the present IB-LBM solver is extended to the flow simulation at moderate Reynolds numbers $Re = O(10^3)$. The pitching plate at $Re = 5000$ (Garmann and Visbal, 2011) is chosen as the benchmark. In this part, two sets of starting styles are adopted which are denoted as Motion-I and Motion-II respectively and

21

the motion style follows

$$\alpha = \frac{\Omega_0}{2a} \ln \left[\frac{\cosh(a(\tau - \tau_1)) \cosh(a(\tau - \tau_4))}{\cosh(a(\tau - \tau_2)) \cosh(a(\tau - \tau_3))} \right], \tag{22}$$

where a relates to the smoothness of the initial stage and Ω_0 denotes the largest pitching rate. In the definition of the pitching angle, τ_i controls the hold time of the motion and follows

$$\tau_1 = \text{start time}, \quad \tau_2 = \tau_1 + \frac{\alpha_0}{\Omega_0}, \quad \tau_3 = \tau_2 + \Delta\tau, \quad \tau_4 = \tau_3 + \frac{\alpha_0}{\Omega_0}, \tag{23}$$

where α_0 is the amplitude of the pitching angle. In the present simulation, for Motion-I and Motion-II, the parameters are defined as

$$\text{Motion-I} : \Omega_0 = 0.4, \tau_1 = 1.6, \alpha_0 = \frac{\pi}{4}, \Delta\tau = 1.121, a = 2;$$
$$\text{Motion-II} : \Omega_0 = 0.4, \tau_1 = 1.6, \alpha_0 = \frac{\pi}{4}, \Delta\tau = 1.121, a = 11. \tag{24}$$

As shown in Fig. 16(a), for relatively smooth Motion-I, the strong LEV can be observed because of the rapid change of the angle of attack (AoA). At the present moderate $Re = 5000$, the secondary structure also exists around the leading edge of the plate due to the formation of LEV. With the increase of the pitching angle, the stability of the wake flow is destroyed and the vortex sheet breaks into several small separated vortices. At the same time, the scale of the LEV increases and re-attaches to the plate, as it can be seen in Fig. 16(b). When the anti-direction pitching occurs, the behaviours of the boundary layer on the top surface of the plate become complex, which makes the characteristics of the force on the plate more complicated, as shown in Fig. 17. With the larger pitching rate in Motion-II, the flow behaviour around the leading edge of the plate at the pitching-increasing stage shows similarity with that observed for Motion-I. Because of the rapid change of the pitching angle, the destruction of the vortex sheet becomes more obvious and the wake flow becomes complex in Figs. 18(a) to 18(c). In addition, the irregular flow field results in the complicated trend of the force coefficients, especially in the pitching-decreasing stage in Fig. 19. According to the comparisons in Figs. 17 and 19, the predictions of the force and moment on the plate agree well with the previous ones with the compressible NS solver in Garmann and Visbal (2011) and the adaptive incompressible NS solver in Liu and Hu (2018).
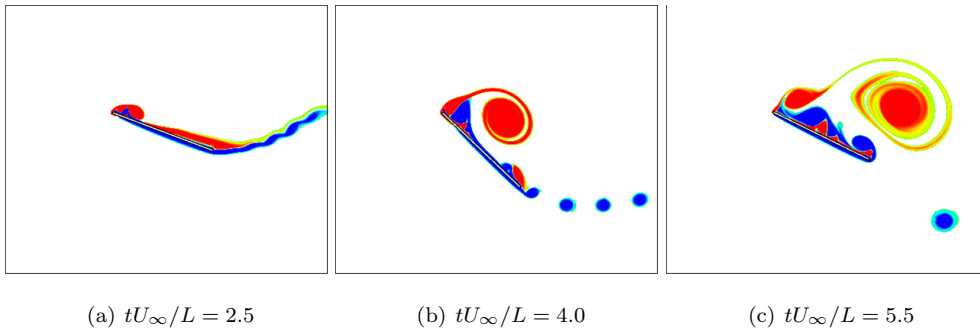

(a) $tU_\infty/L = 2.5$ (b) $tU_\infty/L = 4.0$ (c) $tU_\infty/L = 5.5$

Fig. 16. Flow field around the pitching plate at $Re = 5000$ for Motion-I.

(a) C_d (b) C_l (c) C_m
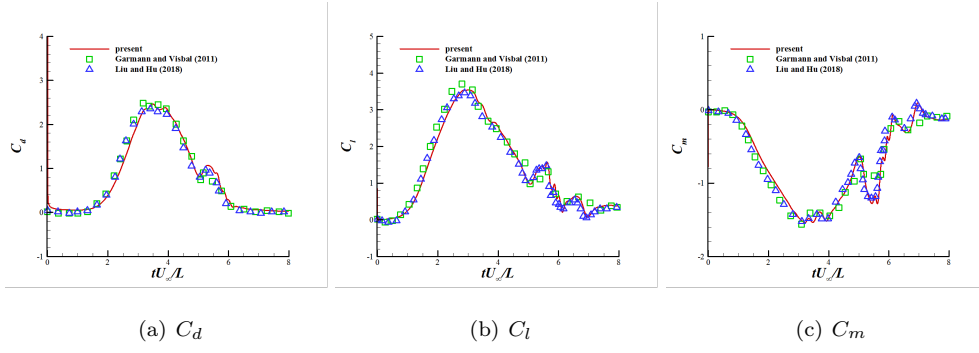
Fig. 17. Hydrodynamic force on the pitching plate at $Re = 5000$ for Motion-I.

(a) $tU_\infty/L = 2.5$ (b) $tU_\infty/L = 4.0$ (c) $tU_\infty/L = 5.5$
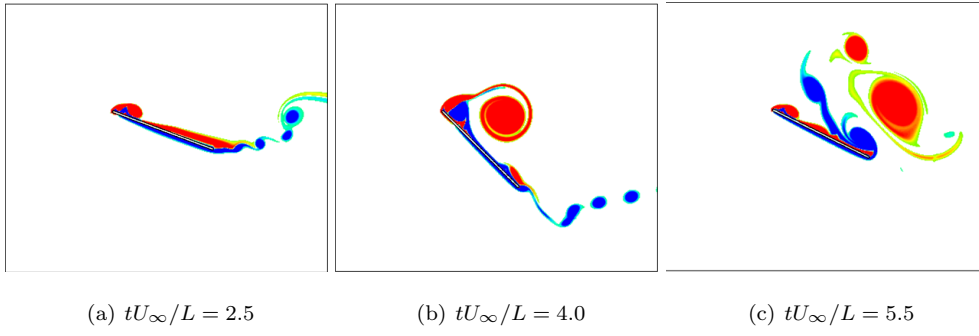
Fig. 18. Flow field around the pitching plate at $Re = 5000$ for Motion-II.

(a) C_d (b) C_l (c) C_m
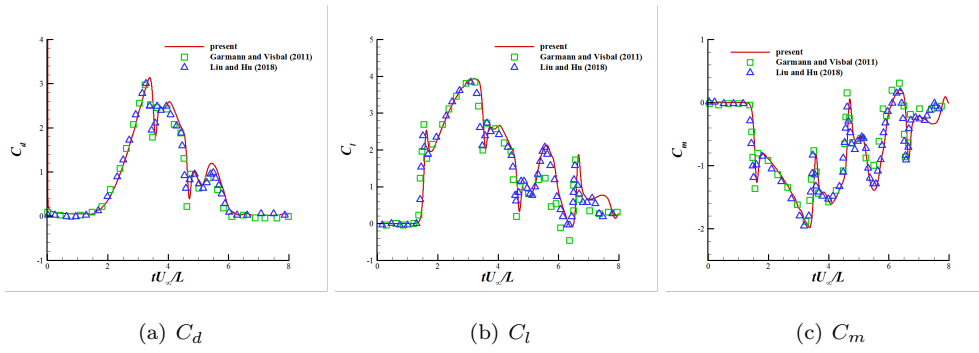
Fig. 19. Hydrodynamic force on the pitching plate at $Re = 5000$ for Motion-II.

4.6 Vortex induced vibration of a circular cylinder

After performance confirmation about the moving boundary with prescribed motions, the present IB-LBM solver is further extended to fluid-structure interactions in this and the next subsections.

Firstly, in this subsection, the Vortex Induced Vibration (VIV) of a circular cylinder with one Degree of Freedom (DoF) in the y direction is simulated. According to Wang and Yeung (2016), the mass ratio m^* is defined as $m^* = m/(\rho D^2)$ for the cylinder with the mass of m and density of ρ, and Re is defined with the inflow velocity U_∞ and the diameter of the cylinder D. In addition, the stiffness k is added to restrict the oscillation of the cylinder, leading to the definition of the reduced velocity $U^* = U_\infty/(fD)$, where f denotes the natural frequency $2\pi f = \sqrt{k/m}$.

In Fig. 20, the non-dimensional Y displacement as the function of U^* with $m^* = 2.0$ and $Re = 150$ is shown and compared with the previous results in Ahn and Kallinderis (2006) and Wang and Yeung (2016). As it can be observed, the overall agreement between the present results and the previous ones are satisfactory. When U^* is small, the larger stiffness of the restriction limits the motion of the cylinder. In this case, the motion amplitude of the cylinder is small and the flow pattern of the wake shares similarity with that of the stationary cylinder, as shown in Fig. 21(a). With the increase of U^*, a sudden increase of the motion amplitude can be observed and its value reaches about $Y_{c-max}/D = 0.56$. Because of the oscillation with large amplitude, the wake flow of the cylinder changes to the $2S$ mode, where two sets of isolated vortices are shed into the wake in one oscillation cycle in Fig. 21(b). With a further increase of U^*, the motion amplitude decreases and the flow pattern of the wake changes back to the normal mode. With $U^* = 8$, the frequency of the vortex shedding deviates from the natural frequency of the cylinder. In this case, the motion amplitude of the cylinder decreases to its minimal value of around 0.08.
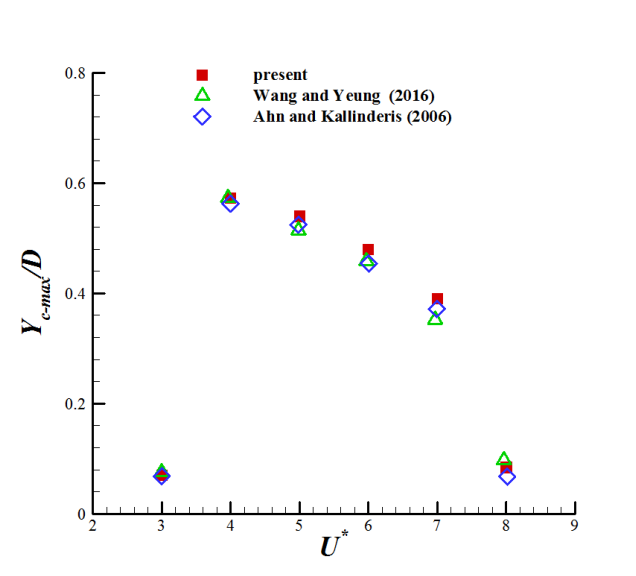

Fig. 20. VIV amplitude of the cylinder with $m^* = 2.0$ and $Re = 150$.

It is well known that the weak coupling strategy is not unconditionally stable, which could have a stability issue when the density ratio is small, i.e., the structure is much lighter than the fluid and the added mass dominates the motion of the body. When the traditional incompressible NS solver is adopted, to achieve a stable simulation, either a small time step or a strong coupling strategy is essential. It is obvious that both methods to remedy the stability issue require considerable computational cost due to the small time step or
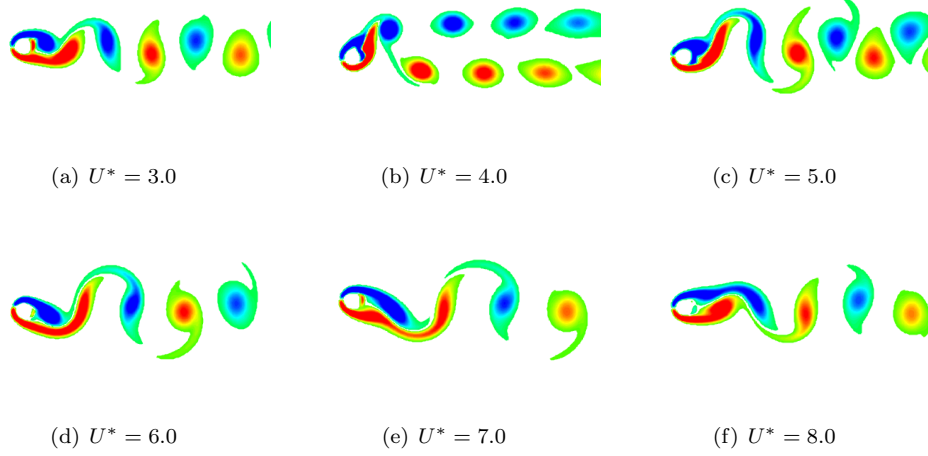
(a) $U^* = 3.0$ (b) $U^* = 4.0$ (c) $U^* = 5.0$

(d) $U^* = 6.0$ (e) $U^* = 7.0$ (f) $U^* = 8.0$

Fig. 21. Flow field around the cylinder with $m^* = 2.0$ and $Re = 150$.

the requirement for sub-cycles in the strong coupling strategy. In the present IB-LBM solver, because of the introduction of the multi-grid based adaptive strategy to resolve the fluid flow, the flow field is predicted with multi-time scales, i.e., 1 step in the coarse grid followed by 2 sub-steps in the fine grid. This manner is equivalent to the "refinement in time" strategy. Therefore, the sub-step integrator in the present model is expected to improve the numerical stability. At the same time, the fine grid in the present adaptive framework covers a small part of the global domain, which only introduces little additional workload for the sub-step computation. To demonstrate such attractive feature, the VIV of a cylinder with two DoFs in the x and y directions and a low density ratio of $m^* = 4/\pi$ at $Re = 200$ is simulated. Further, the damping term is added to the motion of the cylinder with $\zeta = \frac{c}{2\sqrt{km}}$.

As shown in Fig. 22, because of the existence of the mean drag, the mean location of the cylinder moves to the downstream side. With the periodical lift, the cylinder experiences the oscillation in the y direction. The X and Y displacements in the x and y directions form the well-known "8-shaping" pattern, and the present prediction of the displacements agrees well with that obtained by the spectral Finite Element model in Blackburn and Karniadakis (1993) and the sharp interface immersed boundary method in Yang et al. (2008). Furthermore, the large motion amplitude in the y direction causes the $2S$ wake of the cylinder, as shown in Fig. 23. Lastly, the force coefficients on the cylinder are compared with the results in Yang et al. (2008). It can be observed from Fig. 24 that the time history of the forces on the cylinder can be also predicted well using the present model.

In the work of Yang et al. (2008), for the density ratio of 1.07, numerical instability occurs using the sharp interface immersed boundary model with the weak coupling strategy. Furthermore, with an improved weak coupling strategy in Kim et al. (2018), the stable numerical simulation has been extended to about $m^* = 0.2$. To check the robustness of the present IB-LBM solver, the cases with $m^* = 0.7, 0.5, 0.3$ are simulated. As shown in Fig. 25, with the decrease of m^*, the mean displacement of the cylinder in the x direction increases, which correlates to the decrease of the stiffness to keep the reduced velocity. Even with $m^* = 0.3$, the present numerical model can also produce a stable prediction about the motion of the cylinder, which confirms the robustness of the solver. Compared with the results in Kim et al. (2018), the present prediction about the mean shift of the cylinder to the downstream side is satisfactory.
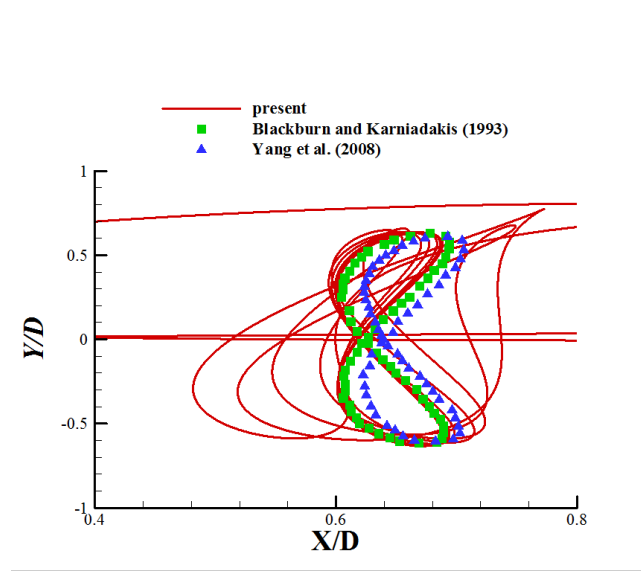
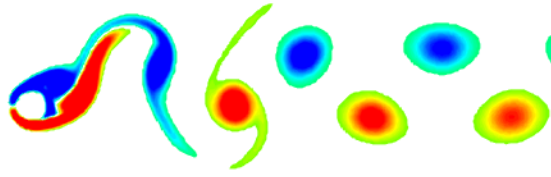**Fig. 22.** Phase plot for the cylinder with $m^* = 4/\pi$ and $Re = 200$.

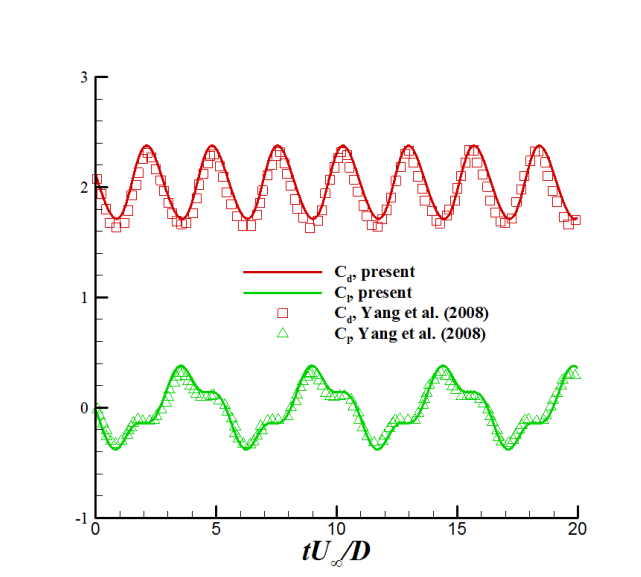**Fig. 23.** Flow field around the cylinder with $m^* = 4/\pi$ and $Re = 200$.

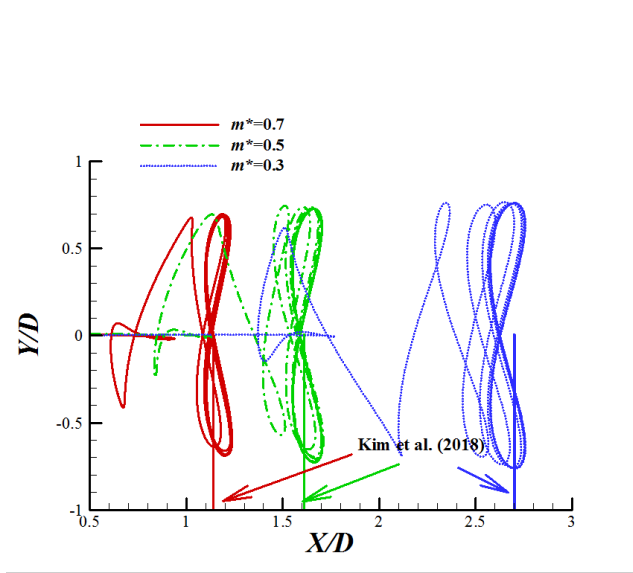**Fig. 24.** Hydrodynamic forces on the cylinder with $m^* = 4/\pi$ and $Re = 200$.

Fig. 25. Phase plot for the cylinder with $m^* = 0.7$ to $m^* = 0.3$.

4.7 Vortex induced rotation of a rectangular cylinder

After the validation about the solid body with a smooth boundary, the vortex induced rotation of a rectangular cylinder is further simulated in this subsection. For such configuration, $I^* = I_s/(\rho_s D^4)$ is adopted to measure the inertial moment of the body, and the aspect ratio of the cylinder is fixed as 0.25. In this subsection, $Re = 250$, $U^* = 40$ and $I^* = 400$ are adopted with two sets of damping ratios $\zeta = 0.25$ and $\zeta = 0.00$. As shown in Fig. 26, with the larger damping ratio, the rotational motion of the cylinder is restricted within $\theta \approx \pm 15°$. In the present work, an initial angular displacement is enforced for an accelerated process of the cylinder reaching its periodic state. Such treatment leads to a phase difference between the present and previous predictions about the angular displacement. Furthermore, because of the numerical inconsistency for St, i.e., the dimensionless frequency of vortex shedding, an additional phase shift also exists for the long term prediction about angular displacement. To match such phase difference, the present results have been shifted in time. As shown in Fig. 26, both the amplitude and the frequency of the present results agree well with the previous ones. From Fig. 27, it can be observed that the sharp corner of the structure and the resulting flow seperation/re-attachment are well captured.

When the damping ratio decreases, the rotational motion of the cylinder increases obviously. With $\zeta = 0.00$, the rotation amplitude reaches about 120°, which is over 10 times larger than that with $\zeta = 0.25$, as shown in Fig. 28. After about 6 periods, the rotational motion of the cylinder reaches its steady state. In Robertson et al. (2003), the numerical model failed to simulate such large-amplitude rotation, while the sharp interface immersed boundary model (Yang and Stern, 2012) removed such restriction. As it can be observed in Fig. 28, the present results are in good agreement with that in Yang and Stern (2012), which confirms the robustness of the present immersed boundary method over the traditional body-fitting model. As shown in Fig. 29, with the large-amplitude rotation, the complex vortex structure can be observed in the wake of the cylinder.
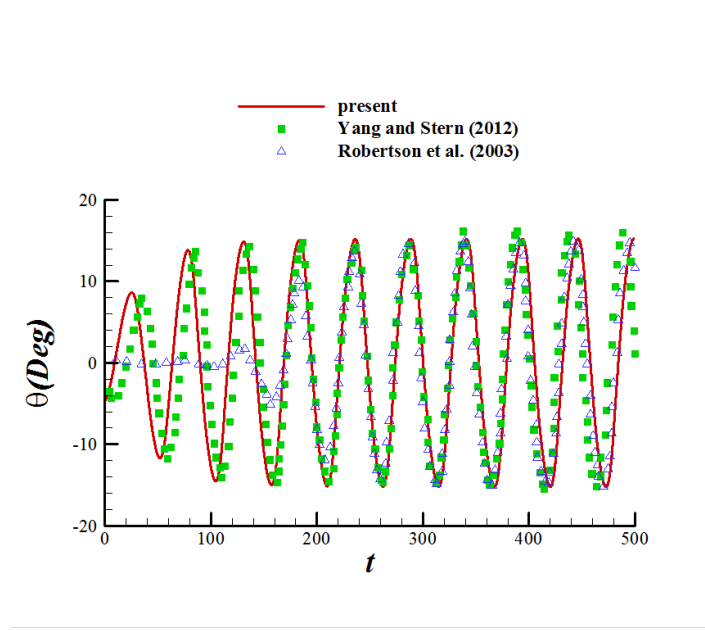
Fig. 26. Angular displacement of the rectangular cylinder with $\zeta = 0.25$.
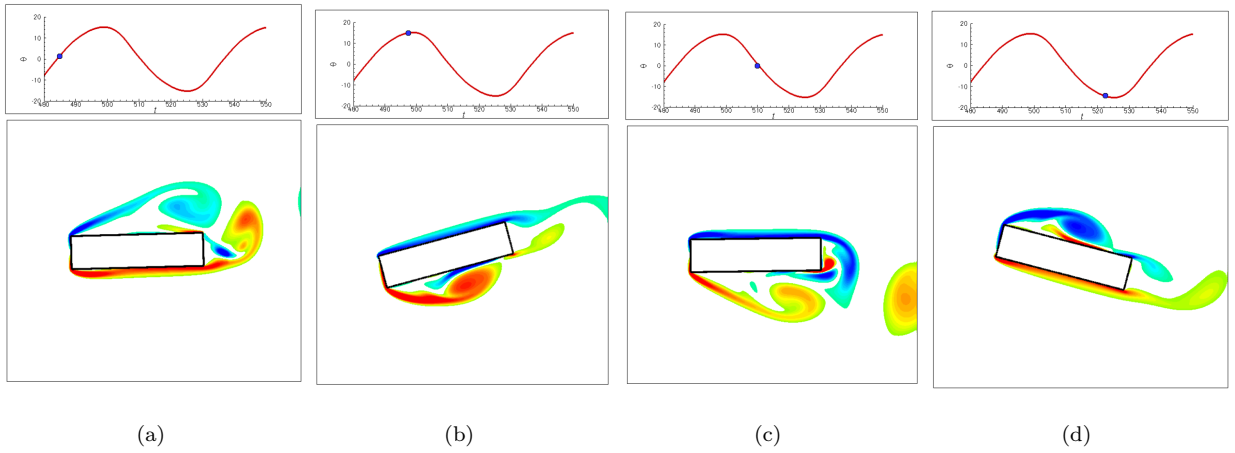

(a)   (b)   (c)   (d)

Fig. 27. Flow field around the rectangular cylinder with $\zeta = 0.25$.

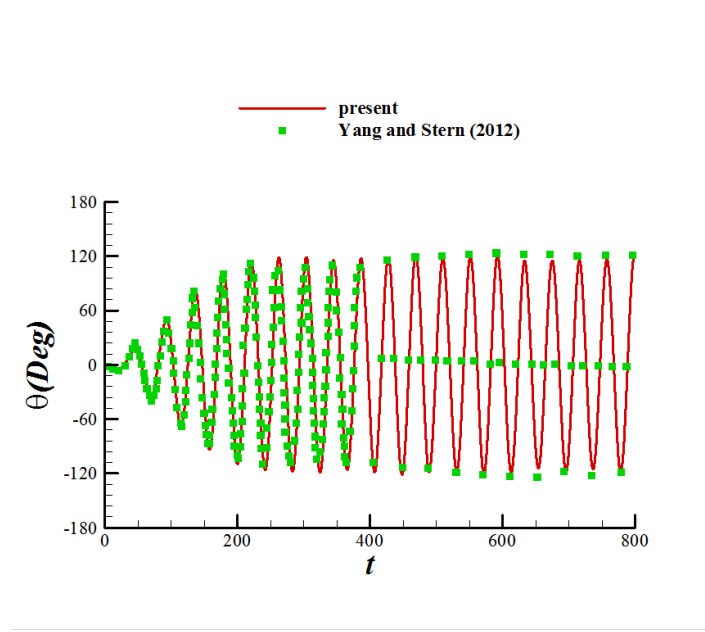**Fig. 28.** Angular displacement of the rectangular cylinder with $\zeta = 0.00$.

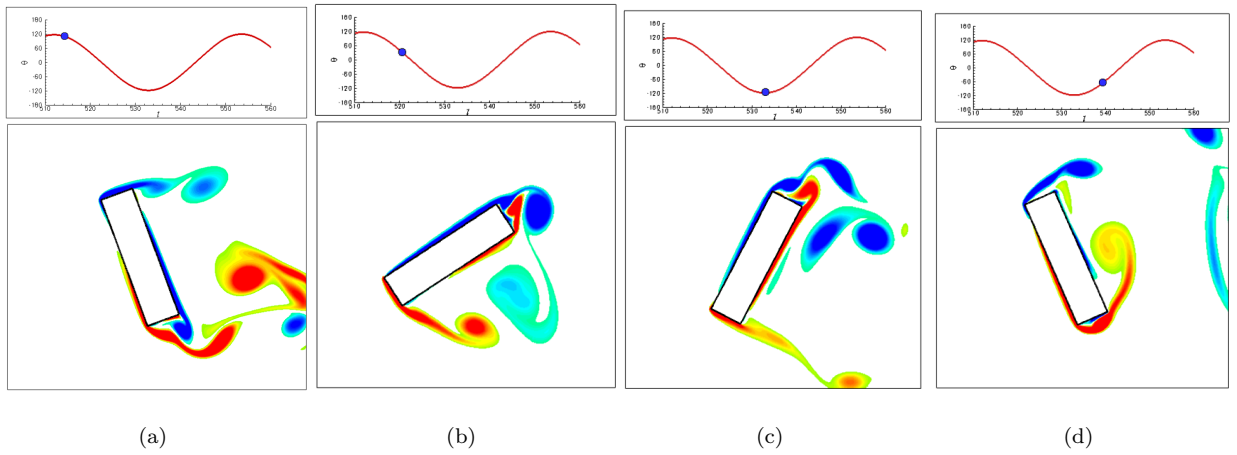<div style="text-align:center">(a)   (b)   (c)   (d)</div>

Fig. 29. Flow field around the rectangular cylinder with $\zeta = 0.00$.

5   Conclusions

In the present work, an efficient Volume of Solid (VOS) based Immersed Boundary (IB) model is built to simulate the fluid flow with complex and moving boundaries. To obtain a unified equation in the entire domain, the VOS based combination strategy for the flow equations and the solid body motion is developed. With the direct forcing algorithm, the no-slip boundary condition is enforced effectively without any special treatment around the structure boundary. Compared with the surface based immersed boundary model, the dependency of the surface discretization on the resolution of the fluid domain is removed, and only the surface mesh, which represents its geometrical characteristics, is sufficient for the model. To solve the interaction between thin-wall structures and fluid flows and further the fluid-structure interaction problems, the present IB model has been coupled with a Lattice Boltzmann Method (LBM), and a local mesh refinement model, together with an adaptive strategy for flow prediction, is developed to improve the efficiency and stability of the model.

Compared with the surface based IB-LBM model, the forcing factor based on the equilibrium velocity has been shown to produce over-corrected flow field in the solid phase and further produces unphysical force oscillation. As a simple remedy about such issue, an optimized forcing factor based on the post-collision state is recommended to control such force oscillation. In addition to the classical benchmark cases, the fluid flow with moderate Re number is also simulated for the Vortex induced Vibration (VIV) problems. The agreement between the present results and the previous well-validated ones confirms the accuracy and the robustness of the present model. Furthermore, even the present numerical model is developed for the 2D situations, it can be easily extended to solve the 3D problems without special difficulties.

References

H. T. Ahn and Y. Kallinderis. Strongly coupled flow/structure interactions with a geometrically conservative ale scheme on general hybrid meshes. *Journal of Computational Physics*, 219(2):671–696, 2006.

Kr. De. Arnab. A diffuse interface immersed boundary method for complex moving boundary problems. *Journal of Computational Physics*, 366:226–251, 2018.

J.A. Baerentzen and H. Aanaes. Signed distance computation using the angle weighted pseudonormal. *IEEE Transactions on Visualization and Computer Graphics*, 11(3):243–253, 2005.

P. A. Berthelsen and O. M. Faltinsen. A local directional ghost cell approach for incompressible viscous flow problems with irregular boundaries. *Journal of Computational Physics*, 227(9):4354–4397, 2008.

H. Blackburn and G. Karniadakis. Two and three-dimensional simulations of vortex-induced vibration of a circular cylinder. In *Proceedings of the Third International Offshore and Polar Engineering Conference, Singapore*, pages 715–720, 1993.

H. D. Chen, O. Filippova, J. Hoch, K. Molvig, R. Shock, C. Teixeira, and R. Zhang. Grid refinement in lattice boltzmann methods based on volumetric formulation. *Physica A: Statistical Mechanics and its Applications*, 362(1):158–167, 2006.

S. Y. Chen, H. D. Chen, D. Martnez, and W. Matthaeus. Lattice boltzmann model for simulation of magneto-hydrodynamics. *Physical Review Letters*, 67(27):3776, 1991.

L. F. Cong, B. Teng, and L. Cheng. Hydrodynamic behavior of two-dimensional tandem-arranged flapping flexible foils in uniform flow. *Physics of Fluids*, 32(2):021903, 2020.

M. Coutanceau and R. Bouard. Experimental determination of the main features of the viscous flow in the wake of a circular cylinder in uniform translation. part 1. steady flow. *Journal of Fluid Mechanics*, 79(2): 231–256, 1977.

H. Dutsch, F. Durst, S. Becker, and H. Lienhart. Low-reynolds-number flow around an oscillating circular cylinder at low keulegan–carpenter numbers. *Journal of Fluid Mechanics*, 360:249–271, 1998.

E. A. Fadlun, R. Verzicco, P. Orlandi, and J. Mohd-Yusof. Combined immersed-boundary finite-difference methods for three-dimensional complex flow simulations. *Journal of Computational Physics*, 161(1):35–60, 2000.

A. Fakhari and T. Lee. Multiple-relaxation-time lattice boltzmann method for immiscible fluids at high reynolds numbers. *Physical Review E*, 87(2):023304, 2013.

J. Favier, A. Revell, and A. Pinelli. A lattice boltzmann–immersed boundary method to simulate the fluid interaction with moving and slender flexible objects. *Journal of Computational Physics*, 261:145–161, 2014.

Z. G. Feng and E. E. Michaelides. Proteus: a direct forcing method in the simulations of particulate flows. *Journal of Computational Physics*, 202(1):20–51, 2005.

D. J. Garmann and M. R. Visbal. Numerical investigation of transitional flow over a rapidly pitching plate. *Physics of Fluids*, 23(9):094106, 2011.

D. Goldstein, R. Handler, and L. Sirovich. Modeling a no-slip flow boundary with an external force field. *Journal of Computational Physics*, 105(2):354–366, 1993.

S. Gsell and J. Favier. Direct-forcing immersed-boundary method: A simple correction preventing boundary slip error. *Journal of Computational Physics*, 435:110265, 2021.

Z. Guo, C. Zheng, and B. Shi. Discrete lattice effects on the forcing term in the lattice boltzmann method. *Physical Review E*, 65(4):046308, 2002.

R. N. Hua, L. D. Zhu, and X. Y. Lu. Dynamics of fluid flow over a circular flexible plate. *Journal of fluid mechanics*, 759:56–72, 2014.

W. X Huang and H. J. Sung. Improvement of mass source/sink for an immersed boundary method. *International Journal for Numerical Methods in Fluids*, 53(11):1659–1671, 2007.

W. X. Huang, C. B. Chang, and H. J. Sung. An improved penalty immersed boundary method for fluid–flexible body interaction. *Journal of Computational Physics*, 230(12):5061–5079, 2011.

S. Jafari, R. Yamamoto, and M. Rahnama. Lattice-boltzmann method combined with smoothed-profile method for particulate suspensions. *Physical Review E*, 83(2):026702, 2011.

S. Kang, G. Iaccarino, F. Ham, and P. Moin. Prediction of wall-pressure fluctuation in turbulent flows with an immersed boundary method. *Journal of Computational Physics*, 228(18):6753–6772, 2009.

S. K. Kang and Y. A. Hassan. A comparative study of direct-forcing immersed boundary-lattice boltzmann methods for stationary complex boundaries. *International Journal for Numerical Methods in Fluids*, 66(9): 1132–1158, 2011.

J. Kim, D. Kim, and H. Choi. An immersed-boundary finite-volume method for simulations of flow in complex geometries. *Journal of Computational Physics*, 171(1):132–150, 2001.

W. Kim, I. Lee, and H. Choi. A weak-coupling immersed boundary method for fluid–structure interaction with low density ratio of solid to fluid. *Journal of Computational Physics*, 359:296–311, 2018.

P. Lallemand and L. S. Luo. Theory of the lattice boltzmann method: Dispersion, dissipation, isotropy, galilean invariance, and stability. *Physical Review E*, 61(6):6546, 2000.

G. J. Li and X. Y. Lu. Force and power of flapping plates in a fluid. *Journal of fluid Mechanics*, 712:598–613, 2012.

R. Y. Li, C. M. Xie, W. X. Huang, and C. X. Xu. An efficient immersed boundary projection method for flow over complex/moving boundaries. *Computers and Fluids*, 140:122–135, 2016.

C. Liu and C. H. Hu. An efficient immersed boundary treatment for complex moving object. *Journal of Computational Physics*, 274:654–680, 2014.

C. Liu and C.H. Hu. An adaptive multi-moment fvm approach for incompressible flows. *Journal of Computational Physics*, 359:239–262, 2018.

A. P. Maertens and G. D. Weymouth. Accurate cartesian-grid simulations of near-body flows at intermediate reynolds numbers. *Computer Methods in Applied Mechanics and Engineering*, 283:106–129, 2015.

R. Mittal, H. Dong, M. Bozkurttas, F. M. Najjar, A. Vargas, and A. von Loebbeckea. A versatile sharp interface immersed boundary method for incompressible flows with complex boundaries. *Journal of Computational Physics*, 227(10):4825–4852, 2008.

Y. Nakayama and R. Yamamoto. Simulation method to resolve hydrodynamic interactions in colloidal dispersions. *Physical Review E*, 71(3):036707, 2005.

D. Pan. An immersed boundary method for incompressible flows using volume of body function. *International Journal for Numerical Methods in Fluids*, 50(6):733–750, 2006.

Z. R. Peng, H. B. Huang, and X. Y. Lu. Collective locomotion of two closely spaced self-propelled flapping plates. *Journal of Fluid Mechanics*, 849:1068–1095, 2018a.

Z. R. Peng, H. B. Huang, and X. Y. Lu. Collective locomotion of two self-propelled flapping plates with different propulsive capacities. *Physics of Fluids*, 30(11):111901, 2018b.

C. S. Peskin. Flow patterns around heart valves: a numerical method. *Journal of Computational Physics*, 10 (2):252–271, 1972.

A. Pinelli, I. Z. Naqavi, U. Piomelli, and J. Favier. Immersed-boundary methods for general finite-difference and finite-volume navier–stokes solvers. *Journal of Computational Physics*, 229(24):9073–9091, 2010.

Y. H. Qian, D. d'Humières, and P. Lallemand. Lattice bgk models for navier-stokes equation. *EPL (Europhysics Letters)*, 17(6):479, 1992.

I. Robertson, L. Li, S. J. Sherwin, and P. W. Bearman. A numerical study of rotational and transverse galloping rectangular bodies. *Journal of Fluids and Structures*, 17(5):681–699, 2003.

M. Rohde, D. Kandhai, J. J. Derksen, and H. E. A. van den Akker. A generic, mass conservative local grid refinement technique for lattice-boltzmann schemes. *International Journal for Numerical Methods in Fluids*, 51(4):439–468, 2006.

E. Rossi, A. Colagrossi, B. Bouscasse, and G. Graziani. The diffused vortex hydrodynamics method. *Communications in Computational Physics*, 18(2):351–379, 2015.

U. Senturk and A. Smits. Numerical simulations of the flow around a square pitching panel. *Journal of Fluids and Structures*, 76:454–468, 2018.

J. H. Seo and R. Mittal. A sharp-interface immersed boundary method with improved mass conservation and reduced spurious pressure oscillations. *Journal of Computational Physics*, 230(19):7347–7363, 2011.

K. Suzuki and T. Inamuro. Effect of internal mass in the simulation of a moving body by the immersed boundary method. *Computers and Fluids*, 49(1):173–187, 2011.

K. Taira and T. Colonius. The immersed boundary method: a projection approach. *Journal of Computational Physics*, 225(2):2118–2137, 2007.

F. B. Tian, H. X. Luo, L. Zhu, J. C. Liao, and X. Y. Lu. An efficient immersed boundary-lattice boltzmann method for the hydrodynamic interaction of elastic filaments. *Journal of Computational Physics*, 230(19): 7266–7283, 2011.

Y. Tseng and J. H. Ferziger. A ghost-cell immersed boundary method for flow in complex geometry. *Journal of Computational Physics*, 192(2):593–623, 2003.

M. Uhlmann. An immersed boundary method with direct forcing for the simulation of particulate flows. *Journal of Computational Physics*, 209(2):448–476, 2005.

L. Wang and R. W. Yeung. On the performance of a micro-scale bach-type turbine as predicted by discrete-vortex simulations. *Applied Energy*, 183:823–836, 2016.

Y. Wang, C. Shu, C. J. Teo, and J. Wu. An immersed boundary-lattice boltzmann flux solver and its applications to fluid–structure interaction problems. *Journal of Fluids and Structures*, 54:440–465, 2015.

Y. Wang, C. Shu, C. J. Teo, and L. M. Yang. An efficient immersed boundary-lattice boltzmann flux solver for simulation of 3d incompressible flows with complex geometry. *Computers and Fluids*, 124:54–66, 2016.

[680] Z. Wang, J. Fan, and K. Luo. Combined multi-direct forcing and immersed boundary method for simulating flows with moving particles. *International Journal of Multiphase Flow*, 34(3):283–302, 2008.

[682] G. D. Weymouth and K. P. Yue. Boundary data immersion method for cartesian-grid simulations of fluid-body interaction problems. *Journal of Computational Physics*, 230(16):6233–6247, 2011.

[684] J. Wu and C. Shu. Implicit velocity correction-based immersed boundary-lattice boltzmann method and its applications. *Journal of Computational Physics*, 228(6):1963–1979, 2009.

[686] L. Xu, F. B. Tian, J. Young, and J. C. S. Lai. A novel geometry-adaptive cartesian grid based immersed boundary lattice boltzmann method for fluid structure interactions at moderate and high reynolds numbers. *Journal of Computational Physics*, 375:22–56, 2018.

[689] S. Xu and Z. J. Wang. An immersed interface method for simulating the interaction of a fluid with moving boundaries. *Journal of Computational Physics*, 216(2):454–493, 2006.

[691] J. M. Yang and E. Balaras. An embedded-boundary formulation for large-eddy simulation of turbulent flows interacting with moving boundaries. *Journal of Computational Physics*, 215(1):12–40, 2006.

[693] J. M. Yang and F. Stern. A simple and efficient direct forcing immersed boundary framework for fluid–structure interactions. *Journal of Computational Physics*, 231(15):5029–5061, 2012.

[695] J. M. Yang, S. Preidikman, and E. Balaras. A strongly coupled, embedded-boundary method for fluid–structure interactions of elastically mounted rigid bodies. *Journal of Fluids and Structures*, 24(2):167–182, 2008.

[697] X. Zhao, Z. Chen, L. Yang, N. Liu, and C. Shu. Efficient boundary condition-enforced immersed boundary method for incompressible flows with moving boundaries. *Journal of Computational Physics*, 441:110425, 2021.